Shaft Efficiency Measurements of a Fully Scaled Turbine in a Short Duration Facility

by

Rory Keogh

B.S. Mechanical Engineering
University College Galway, Ireland
1989

Submitted to the Department of Aeronautics and Astronautics
in partial fulfillment of the requirements for the degree of

Master of Science in Aeronautics and Astronautics

at the

MASSACHUSETTS INSTITUTE OF TECHNOLOGY

February 1998

Author...
Department of Aeronautics and Astronautics
January 22, 1998

Certified by ....
Gerald R. Guenette
Principal Research Engineer
Gas Turbine Laboratory
Thesis Supervisor

Accepted by..
Professor Jaime Peraire
Chairman, Department Committee on Graduate Students

Shaft Efficiency Measurements of a Fully Scaled Turbine in a Short Duration Facility

by

Rory Keogh

Submitted to the Department of Aeronautics and Astronautics
on January 22, 1998, in partial fulfillment of the
requirements for the degree of
Master of Science in Aeronautics and Astronautics

Abstract

Short duration blowdown-type turbomachinery test facilities offer the potential for low cost, high accuracy testing of axial flow turbines. This thesis outlines the work done to date using MIT the Blowdown Turbine Facility to measure the aerodynamic efficiency of a fully scaled single stage turbine. The differences between the non-adiabatic nature of short duration rigs and adiabatic testing in steady state rigs is explored and shown to be on the order of 0.25% of the adiabatic efficiency. The uncertainty associated with this correction is shown to be smaller than the uncertainty from other turbine measurements.

The power produced by the turbine is measured directly and the ideal power is determined by measuring the turbine mass flow, pressure ratio and inlet temperature. This investigation focused on the power measurement and the mass flow measurement of the turbine stage.

Thesis Supervisor: Gerald R. Guenette
Title: Principal Research Engineer
Gas Turbine Laboratory

Acknowledgments

Contents

List of Figures

List of Tables

Chapter 1

Introduction

1.1 Motivation

Since the development of the jet engine the aerodynamic performance of turbines has increased enormously, with polytropic efficiencies now in the low 90% range. At the same time, turbine inlet temperatures have risen on the order of $1000°K$ through the development of extraordinary turbine blade and disk materials as well as sophisticated internal and external blade cooling schemes. Thus, modern engine designs produce much higher power per unit mass with a substantial increase in efficiency as compared to their predecessors. The efficiency increase has come through improved design techniques based on better understanding of the fluid mechanics of turbines and the power of computational tools. Under pinning all of this are empirical observations acquired through many years of extensive testing on engines, rigs, and sub- scale experiments.

The use of film cooling to increase turbine inlet temperatures has lead to a trade-off between efficiency and the power per unit mass flow (or the thrust to weight ratio) developed by the engine. It is also a trade-off that is made by designers based on empirical approaches. The impact of film cooling on aerodynamic efficiency is an area where computational tools have yet to make a significant impact, and as such can benefit from continued turbine testing. However the high cost of such turbine testing has all but stopped turbine research

at this level. Even engine development programs have been greatly affected; a military engine program may include only one, or even zero turbine test rigs. Thus, the only test a new turbine design may see is in an engine. Unfortunately, the aerodynamic efficiency measurement accuracy currently possible in a full-scale engine is on the order of 1% to 2%, which is considerably less than that demanded of modern turbine design systems. This results in a situation where design improvements may not be attempted if it is believed that the change cannot be evaluated by experiment. In the case of large gas turbine used for power generation, turbine test rigs are not practical because of the immense size and power requirements involved. Turbines can only be tested in service and this leads designers to conservative turbine designs, as it is better to have slightly a inefficient turbine than none at all.

A similar situation existed for turbine heat transfer and cooling. However, during the 1980s a new technology based on transient testing techniques was developed which provided highly accurate and detailed turbine measurements at relatively low cost[4]. The technique is based primarily on the realization that the time scales characteristic of the physics within a turbine are on the order of hundreds of microseconds. With instrumentation of adequate time response, test less than a second long may be sufficient to establish steady state behavior for the turbine.

Although instantaneous power generated during a short duration test may be quite high (several megawatts), the energy required is quite low. Also, through the use of scaling, the turbine inlet temperature can be reduced significantly, as can the rotor tip velocity. These three factors reduce the construction, maintenance, and power costs of turbine testing. Safety margins are also improved for the tests, thus eliminating the need for redundancy of critical systems. To date, the work in short duration turbine test facilities has been aimed predominantly at heat transfer and cooling studies. This thesis addresses the question of aerodynamic performance testing of turbines in short duration facilities using the shaft efficiency approach.

1.2 Thesis Outline

This thesis is organized into the following chapters. Chapter 2 describes the Blowdown Turbine Facility. A brief description of the operation of the test rig is presented. Also, all of the major modifications to the facility are briefly discussed. The fabrication of the new turbine test section and associated hardware is discussed. Modifications to the eddy current brake and the installation of a critical flow venturi to measure mass flow are discussed. Chapter 3 outlines in detail the design and calibration of the eddy current brake. Chapter 4 deals with the mass flow measurement. A background to the critical flow venturi is provided as well as the correction that is required to account for the transient nature of the test. The uncertainty analysis for the mass flow measurement is presented. Chapter 5 outlines how the measurements are used to calculate the turbine efficiency. The difference between short-duration testing and steady adiabatic test rigs is also analyzed. The uncertainty analysis for the efficiency is presented. Chapter 6 presents a summary of the work done to date.

Chapter 2

Facility Description

2.1 Introduction

This chapter describes the blowdown turbine test facility, on which the experimental work presented in this thesis was conducted. Modifications to the MIT blowdown turbine facility such as the eddy current brake torque meter and the mass flow meter are emphasized. The wind tunnel and its principle of operation, the instrumentation and the data acquisition system are also presented.

2.2 The MIT Blowdown Turbine Facility

The Blowdown Turbine facility is a fully scaled transient wind tunnel capable of fully simulating the non-dimensional flow conditions for modern transonic axial turbines complete with film cooling. Table 2.1 shows how the main operating parameters of the facility compare with those of the turbine being studied. All of the non-dimensional parameters relevant to turbine aerodynamics and heat transfer are simulated.

The useable test time for the rig is approximately 500 milliseconds for the current turbine configuration. This time is large compared to the time scales of the flow and to the rotor to stator passing frequency (see Epstein[1]) so the turbine operates in a quasi-steady state.

The specific heat ratio, γ, an important parameter for compressible flow, is matched by

Table 2.1: MIT Blowdown Turbine Scaling

Parameters	Full Scale Engine	MIT BDT
Working Fliud	Air	$Argon - CO_2$
Ratio of Specific Heats, γ	1.28	1.28
Mean Metal Temperature	1100 K (1521°F)	300 K (81°F)
Metal/Gas Temp. Ratio	0.647	0.647
Inlet Total Temperature	1700 K (2600°F)	464 K (376°F)
True NGV Chord (midspan)	0.146 m	0.0365 m
Reynolds Number	5.6×10^6	5.6×10^6
Inlet Total Pressure	15 atm (224 $psia$)	7 atm (105 $psia$)
Exit Total Pressure	7.43 atm (111 $psia$)	3.47 atm (52 $psia$)
Exit Total Temperature	1470 K (2187°F)	401 K (262°F)
Prandtl Number	0.928	0.742
Design Rotor Speed	3600 rpm	5954 rpm
Design Mass Flow	312 kg/s	23.3 kg/s
Turbine Power Output	91.13 MW	1.26 MW
Test Time	$Continuous$	0.3 sec

using a mixture of CO_2 and Argon. The mixture composition will depend on the turbine inlet temperature for the test, as the specific heat capacity CO_2 has strong temperature dependence.

While the test time is large relative to the time scales of the flow it is very short compared to the thermal time scales of the blades and end walls of the rig. The blades remain at a constant temperature for the test duration. The gas to metal temperature ratio is kept constant so the heat loss to the blades and end walls is the same proportion of turbine enthalpy as in an engine environment. This requirement sets the gas temperature of the main and coolant flows. The Reynolds number similarity determines the turbine inlet pressure.

Table 2.1 shows the distinct advantages of the blowdown turbine test rig. Firstly, because of the lower gas temperature and use of heavier working fluid, the turbine tip speed is only half that of the full-scale engine while maintaining the desired corrected speed (or tip Mach number). As a result of the lower speed, the lower metal temperature, and the short life of the turbine, large factors of safety can be used for the structural design of the turbine.

The reduced pressure and power generated makes the experimental facility safer and easier to operate. Also, the slower rotor speed lessens the requirement on the bandwidth of the high frequency instruments, and the relatively benign environment due to the low gas and metal temperatures enables the use of the heat flux gages described is reference [3].

A schematic of the blowdown turbine facility is shown in Figure 2.1. The main components are the supply tank, fast acting valve, test section, downstream translator, eddy current brake torque meter, mass flow meter and dump tank. Cross-sectional views downstream of the main valve are shown in Figures 2.2 and 2.3.

Concentric cylindrical walls form the flowpath upstream of the test section. Upstream of the Nozzle Guide Vanes is a contraction, which simulates the geometry of the engine combustor exit. Boundary layer bleeds placed upstream of the contraction capture the boundary layer of the upstream flow and ensure that relatively clean flow enters the test section. The turbine pressure ratio is set by a throttle plate, which slides along the tunnel axis to adjust the choked exit flow area. Several tests are generally required in order to fine-tune the pressure ratio.

Before testing, the entire tunnel is evacuated and the supply tank is heated to the desired temperature. Then the fast acting valve is closed and the supply tank is filled with the test gas to the desired test pressure. The eddy current brake and translators are then set to standby mode. The rotor is spun up in vacuum by the drive motor to above the desired test speed. The drive motor is then shut off and slows due to friction. When the rotor speed reaches the preset value, the fast acting valve, eddy current brake, downstream translator, and data acquisition system are activated. The main valve opens in 20-50 milliseconds and the initial transients settle out in about 200 milliseconds. The pressure differences between the supply and dump tanks sustain a test time of approximately 800 milliseconds before the throttle plate unchokes. During the test time the turbine corrected speed and pressure ratio are held constant to better than 1%. The data acquisition system continues to take data for ten minutes to monitor tunnel conditions and to provide data for a post-test transducer calibration.

15

2.3 Facility Modification

As part of the current test program several major redesigns were incorporated into the facility. Firstly, as a result of a change of sponsor, it was decided to design a test section that is a scaled model of a power generation turbine recently introduced into service by ABB. Modifications to the facility to determine the shaft efficiency of the turbine include converting the eddy current brake into a torque meter to measure the shaft power output, and the design and installation of a critical flow venturi as a mass flow meter.

2.3.1 Test Section Redesign

As part of this test program it was decided to design a test section that was of direct interest to the program sponsor. The GT24 is a dual combustor combined cycle engine that recently entered service. The second high-pressure turbine was selected for study because it was of significant interest to ABB and was most compatible to the existing MIT facility.

Scaling

ABB provided MIT with the 3D data files that define the full-scale turbine stage. The model represents the blade and vane in their cold, or room temperature condition. Under engine operating conditions the blades will grow due to thermal expansion. The expansion will be non-uniform because of temperature gradients in the part. Also, the blades will be stretched due to centrifugal loading. For simplicity the blade growth was approximated by uniform expansion, and the blade height was adjusted to give the desired tip clearance. Because the blade is approximately $\frac{1}{4}$ scale it was not feasible to fully scale the blade tolerances. The relative profile tolerances of the scaled blades and vanes are twice that of the full scale geometry.

Design and Fabrication

The design of the new test section is based closely on the ACE turbine that the facility was designed around. The split disk arrangement of the original design was copied. The design

intent of the split disk is to provide a ring that holds the blades. This ring or mini-disk should be inexpensive to replace in the event that the number of blades, or the stagger angle needed to be changed. However, the mini-disk proved to be the next most expensive part to the blades and vanes. In retrospect the split disk design may not be worth while. The seal upstream of the disks and the T-ring downstream of the disks are similar to the previous design. To ensure the hardware fit together, extensive use was made of digital pre-assembly (using ProEngineer) during the design. MAL Tool and Engineering, a contractor to most of the aircraft engine companies, was selected to manufacture the blades and vanes.

The most precise part of the blade is the dovetail profile of the Root; its profile tolerance is ± 0.001 inches. The profile was milled using a tool designed for the MIT profile. The dovetail then serves as datum reference from which all other measurements are made on the part. The root then held the part and the airfoil surfaces were machined using a multi-axis CNC machine to within a few thousandths of an inch of the desired profile. The blades were then polished to their final form by hand. Guillotine gages, which define the maximum profile tolerance at three radial sections, ensure the contour. Feeler gages are used to insure that the blade profile does not fall inside the minimum tolerance.

2.3.2 Eddy Current Brake Torque Meter

The eddy current brake is basically an electrical generator. The motion of a conductor through an applied magnetic field induces an electric current in the conductor and this current in the presence of the magnetic field produces a (Lorentz) force opposing the motion. This force (or torque in rotating geometry) provides the braking required to absorb the power generated by the turbine. The resistive heating of the induced current circulating in the conductor dissipates the power generated in the eddy current brake.

In order to measure the shaft efficiency of the stage it is necessary to measure the torque generated by the turbine. The original eddy current brake as shown in figure 3-4 was attached directly to the main frame. The brake was redesigned in order to meter the torque transmitted from the brake to the main frame.

Figure 3-3 shows the redesigned brake assembly. The magnet coils and the return iron are mounted together on a plate, keeping the same position relative to the rotating drum as in the old design. The motor support was then modified to form a shaft on which the brake assembly is mounted through two radial slim line bearings. The brake assembly is then restrained by two s-beam load cells attached between the motor support and brackets that extend from the rear of the mounting plate through the motor support. The torque generated by the eddy current brake can now be measured. The calibration procedure for the brake is discussed in chapter 4.

2.3.3 Critical Flow Venturi

A critical flow venturi was installed in line with the exit flow path to measure the mass flow rate through the turbine. The nozzle design and upstream duct requirements are based the ANSI standard (reference[10]) for torroidal throat critical flow venturi. Extensive modifications to the facility were required to meet installation requirements for the nozzle.

The main design challenge was to incorporate the required upstream duct length into the facility given the space restrictions. This was accomplished be installing the critical flow venturi and the upstream duct inside the dump tank. A 66 inch extension was added between the dump tank and main frame in order to relocate the eddy current brake and starter motor. Extensions were also required connect the boundary layer bleeds to the dump tank, and to connect the fill system to the supply tank.

Figure 4-6 shows the detailed design of the nozzle. The nozzle was designed and built Flow Systems Inc. of Boulder Colorado and calibrated by Colorado EESI. Figure 4-5 shows the nozzle and upstream duct assembly. Figure 2-1 shows nozzle installed in the facility.

A 50% open area screen is installed at the entrance to upstream duct. This reduces the total pressure non-uniformity caused by the stepped transition from annular to circular cross section around the starter motor. The nozzle was calibrated with the upstream duct and a simulated blockage in place. Flow strengtheners are installed upstream of the throttle plate to ensure that the flow entering the nozzle is swirl free.

18
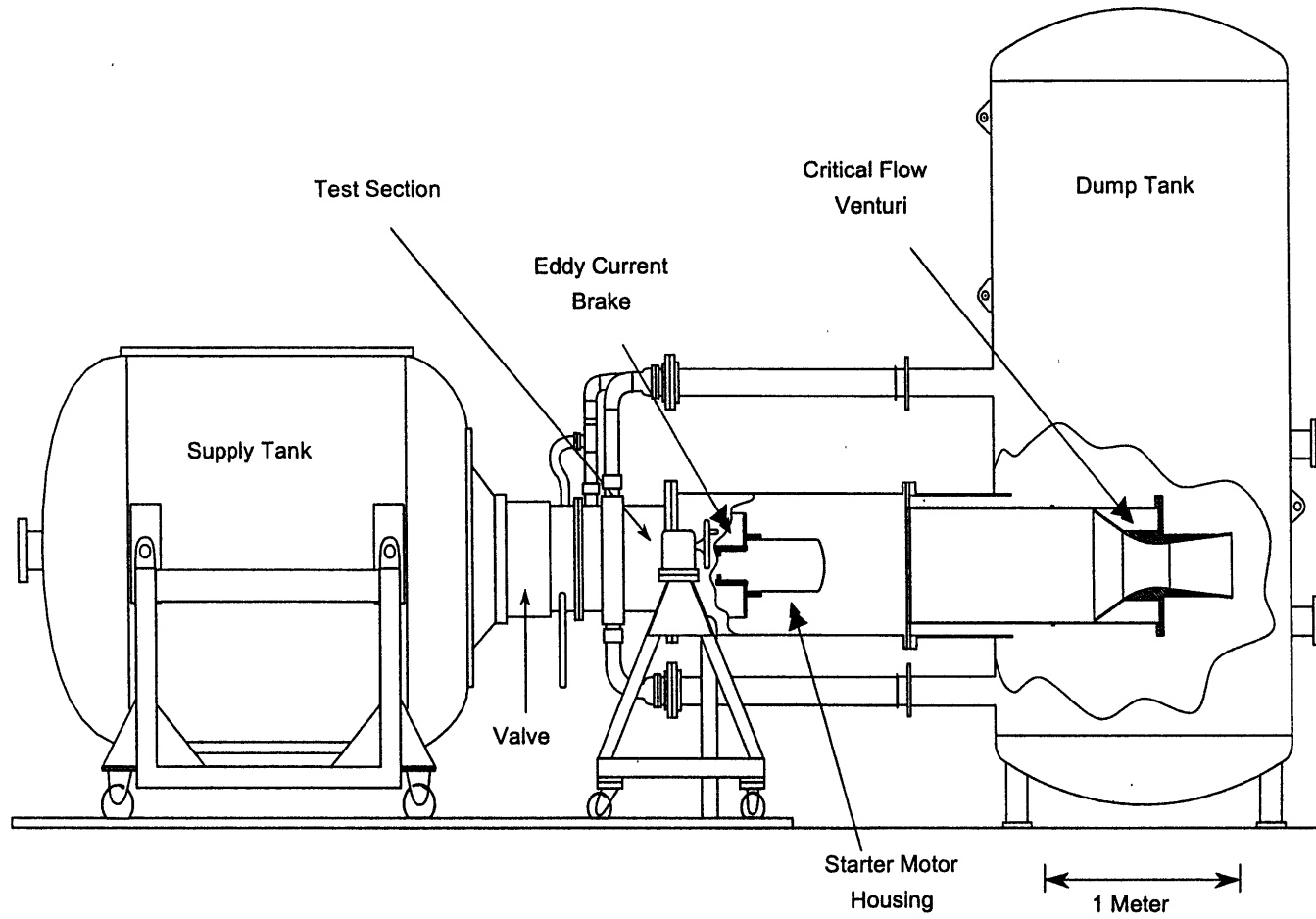
Figure 2-1: Facility Layout

Test Section

Critical Flow
Venturi

Dump Tank

Eddy Current
Brake

Supply Tank

Valve

Starter Motor
Housing

1 Meter

Mass Flow Meter

Turbine Stage

Exhaust to Dump Tank

Inlet

Boundary Layer Bleed

Turbine Disks

Downstream Total Pressure Rake
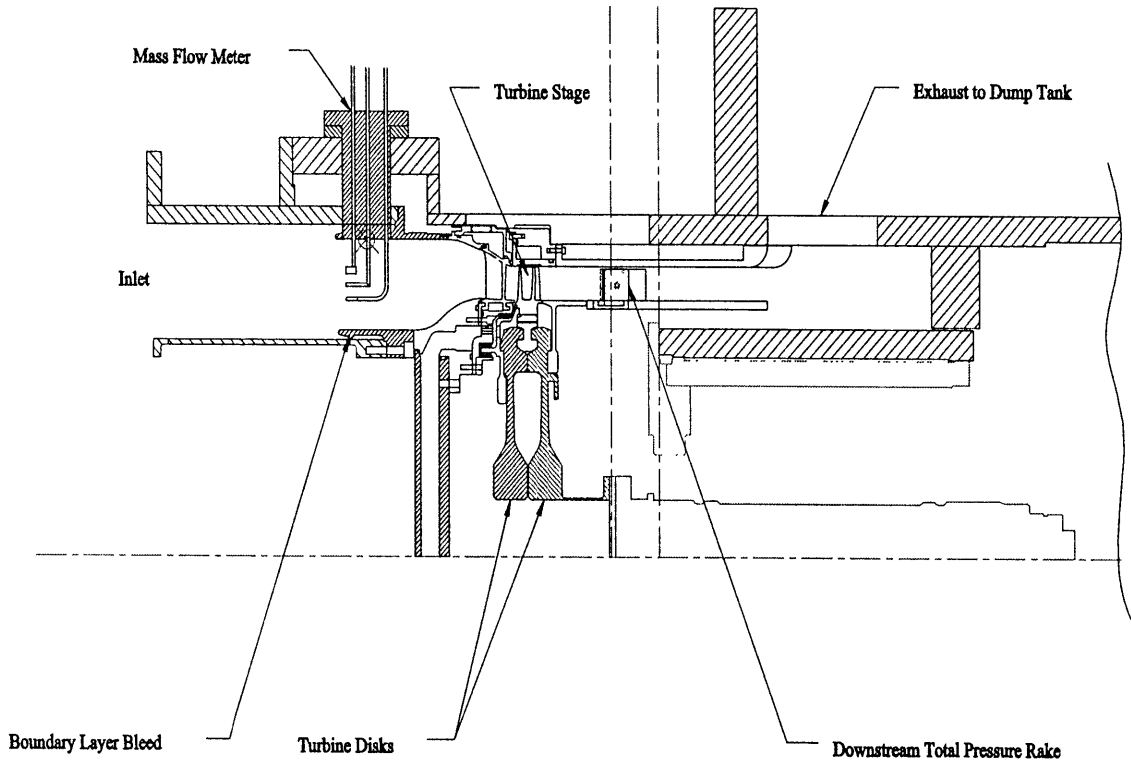
Figure 2-2: Facility Cross Section

20
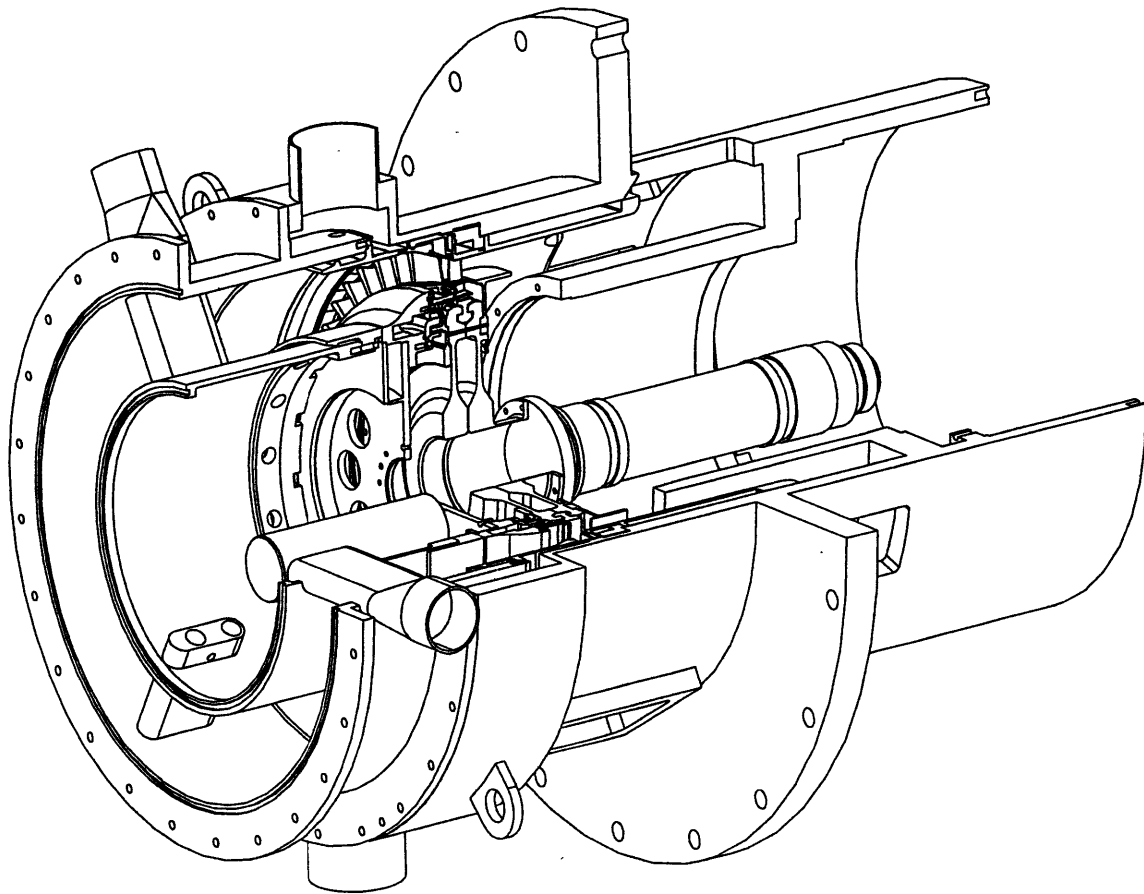
Figure 2-3: Main Frame Cutway
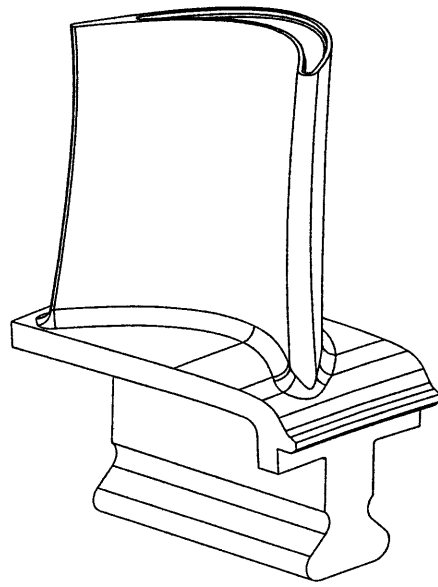
Figure 2-4: Scaled Turbine Blade
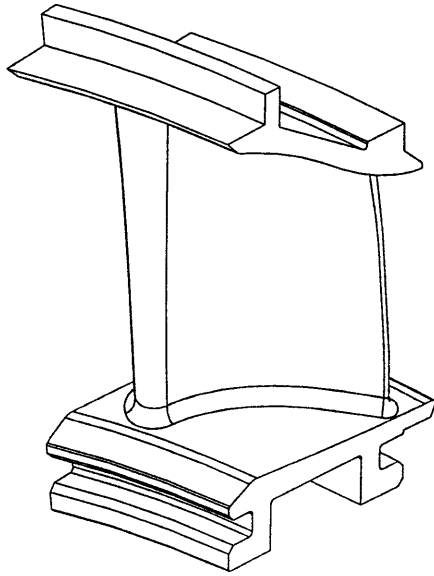
Figure 2-5: Scaled Turbine Vane
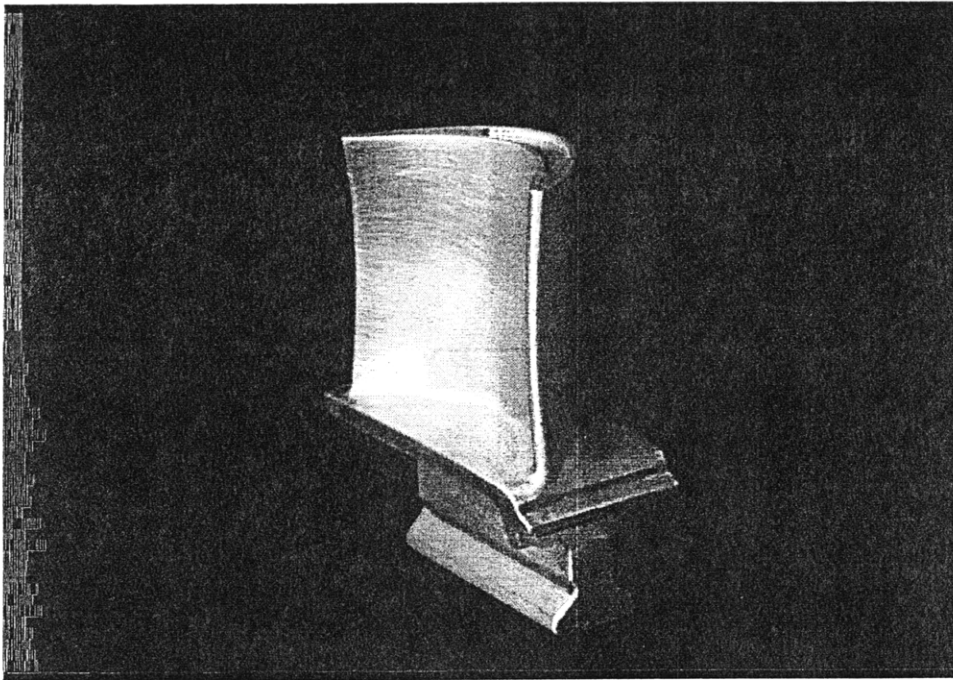
Figure 2-6: Scaled Turbine Blade
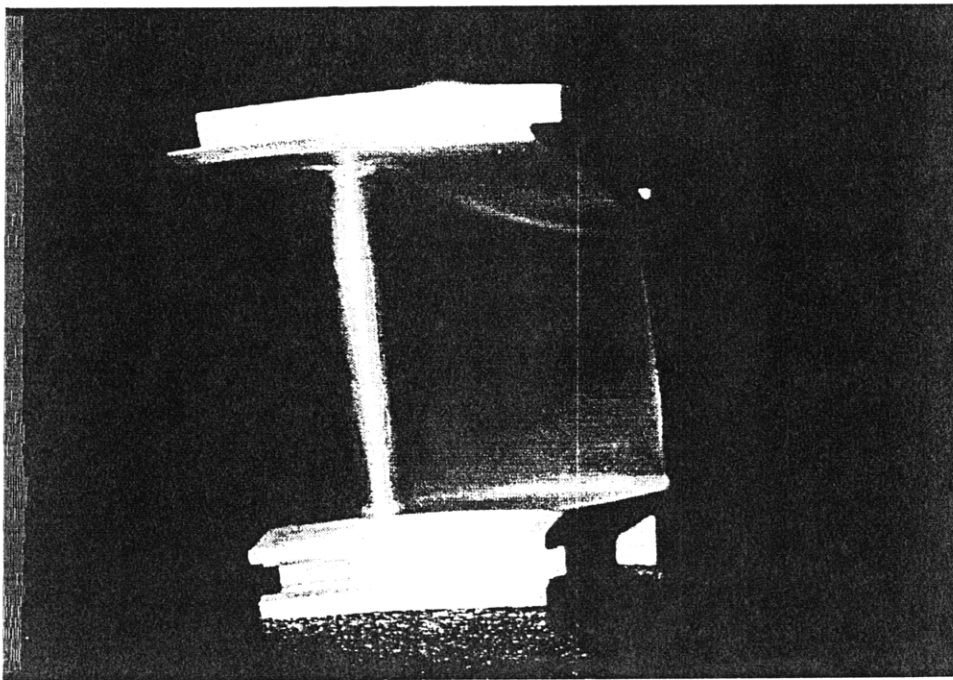
Figure 2-7: Scaled Turbine Vane

Chapter 3

Shaft Power Measurement

3.1 Introduction

A measurement of the shaft power is required to estimate the real work generated by the turbine stage. The shaft power is simply the product of the shaft torque and angular velocity. The eddy current brake, which is used to absorb the power generated by the turbine, has been modified so that the torque transmitted from the brake to the main frame of the facility can be measured directly. The power produced by the turbine can then be expressed as:

$$P = T \cdot \omega + I \cdot \frac{d\omega}{dt} \cdot \omega \qquad (3.1)$$

Where P is the shaft power, T is the torque measured at the brake, ω is the angular speed, and I is the moment of inertia of the rotating components (the blades, disks, shaft, and the brake drum). The frictional losses will be shown to be negligible compared to the other terms. This chapter will first review the design of the old eddy current brake and then outline how it was modified so that the torque can be measured. The calibration of the brake torque meter and rotor inertia will then be described in detail. The shaft speed measurement and the data acquisition system will also be reviewed.

3.2 Eddy Current Brake Design

The eddy current brake theory, development, and design is described in detail by Guenette [3]. The eddy current brake is simple in concept, it is basically an electrical generator. The motion of a conductor through an applied magnetic field induces a current in the conductor, this current in the presence of the same field, generates a (Lorentz) force that opposes the motion of the conductor. In this experiment, this force (or torque in rotating geometry) provides the braking required to absorb the power generated by the turbine. This braking is required in order to maintain the turbine at a desired speed, otherwise the turbine would accelerate over the test duration. The power absorbed appears as resistive heating from the induced current circulating in the moving conductor.

When the magnetic field generated by the induced current is small compared to the applied magnetic field, the braking force is linearly proportional to the velocity past the magnetic poles. As the velocity is increased, the induced field strength grows relative to that of the applied field. This reduces the incremental rise in braking force with speed (i.e., reduces the slope of the torque versus speed curve) until a critical speed, ω_0 is reached. At this point the induced field strength equals that of the applied field and the braking force begins to decrease with increasing speed. A detailed analysis of the brake can be found in Appendix B of reference [3].

A simple model of the basic eddy current brake torque versus speed characteristic is the induction motor which closely approximates the brake behavior up to the critical speed, ω_0:

$$T = kB_0^2 \frac{\omega}{1 + \left(\frac{\omega}{\omega_0}\right)^2} \tag{3.2}$$

Where T is the torque, k is a constant established by the geometry and material properties, B_0 is the applied magnetic field strength, ω is the angular velocity, and ω_0 is the critical velocity at which the induced field strength equals the applied field. The brake was designed so that the critical speed ω_0 is above the turbine operating speed.

The critical speed is a function of geometry and material properties:

$$\omega_0 = \frac{\pi \left(\frac{2g}{\tau}\right)}{\mu \sigma \Delta r} \tag{3.3}$$

where μ is the permeativity of free space, σ is the conductivity of the conductor material, 2g is the gap between adjacent poles of the magnet, τ is the pole pitch of the magnets, r is the center of rotation, and Δ is the thickness of the conductior. The geometric design parameter, k, can be written as

$$k = nA_p\sigma_{eff}\Delta r^2 M \tag{3.4}$$

Where A_p is the cross sectional area of the magnetic pole face normal to the direction of the applied field, n is the number of poles, and M is an empirical field fringing parameter approximately 1.2 to 1.7 (M is Ag/Ap where Ag is the area of the applied field on the drum, per pole).

A cantilever drum design was chosen for the rotating conductor for reasons of simplicity. The eddy current brake configuration is summarized in table 3.1. The moving conductor serves as a heat sink as the power is absorbed by resistive dissipation. The drum is uncooled during the test the temperature rises as the power is absorbed.

The eddy brake magnets are required to provide a 0.7 tesla magnetic field across the 1.25 cm gap, rise from zero to full field strength in 50 milliseconds, and provide a constant field strength for a period of up to two seconds. The brake turn-on time must be compatible with the 50 milliseconds turn-on time of the main valve. The brake must also turn off automatically in order to prevent overheating of the coils and more importantly, the loss drum which is limited to $1200°F$. The switching circuit in figure 3-2 is used to turn on the current.

The power source for the magnets is a 250hp D.C. motor-generator set rated at 250V and 600A at continuous service. This generator was never intended to come up to load in 50 milliseconds, therefore a water cooled 0.4 ohm ballast resistor is used to initially establish the operating point on the generator load line. A vacuum contractor rated at

Table 3.1: Eddy Current Drake Configuration Summary

Design Point	
Power	1,078,000 watts
Speed	6,190 RPM
Loss Drum	
Material	Inconel 718
Physical Properties	
Magnetic permeability	$\mu = 4\pi \cdot 10^{-7} H/m$
Electrical conductivity	$\sigma = 0.801 \cdot 10^{6} \, (\Omega \cdot m)^{-1}$
Density	$\rho = 8.19 g/cc$
Specific Heat	$C_p = 427 J/kg \cdot K$
Configuration	
Mean radius	$r = 0.1619 m$
Thickness	$\Delta = 6.35 \cdot 10^{-3} m$
Axial length (min. active)	$w = 0.1524 m$
Excitation Magnets	
Cores	
Material	Grade M-6 transformer stock and ingot iron
Saturation limit	Approx. 20,000 Gauss
Number of poles	$n = 20$
Pole width (circ.)	$2a = 0.0254$
Pole length (axial)	$2b = 0.1524$
Pole pitch	$\tau = 0.0509$
mechanical airgap	$l_g = 0.0127$
Coils	
Turns	$N = 444$ turns per coil #23AWG magnet wire
Resistance	$R_c = 12$ ohns per coil
Inductance	$L_c = 0.12$ Henrys per coil
Power dissipation	$P_c = 2700$ watts per coil @15A excitation
Machine Characteristics	
Magnet time constant	$\tau_c = 0.01$ sec
Drum effective conductivity	$\sigma_{eff} = 0.721 \cdot 10^{-6} \, (\Omega \cdot m)^{-1}$
Drum axial resistance	$R_D = 3.27 \cdot 10^{-5} \Omega$
Induced current (equivalent axial)	$i_{eq} = 175,00$ amps @ 1 MW dissipation
Drum heating	$\Delta T = 290^{\circ}C$ per 10^6 joules absorbed

50 kV and 150A continuous service is used to switch the magnet coils in parallel with the ballast resistor. Starting from a high load condition, the generator is then able to handle the additional load of the coils with negligible transients.

During brake operation, 800 amps at 200V is drawn from the generator, which has sufficient inertia to provide this overload of current for two seconds. The magnets are de-energized by switching off the shunt field excitation to the generator and allowing the current to decay. This prevents the high voltage arcing problem associated with the opening of a large inductive circuit. Both fuses and a fast acting DC circuit breaker protect the generator. The magnet coils are also fused with a 2 to 4 second time constant. One kilojoule varistors are included to protect the switch and magnetic coils. Isolation amplifiers are used to protect the acquisition system channels monitoring the brake currents and voltages.

3.3   Torque Meter Design

The Eddy Current Brake was redesigned so that the torque transmitted to the brake could be measured during the test. In the old design the magnet assembly was attached to the main frame and the torque was transmitted directly from the brake. The new design assembled the magnets and return-iron together and then mounted the unit on bearings to the main frame. The brake was then restrained using two load cells that measured the forces transmitted to main frame. The load cells were then calibrated as outlined in section 3.4.

The redesign proved to be proved to be mostly a complex mechanical design problem. The original eddy brake was designed at the same time as the rest of the facility, so the main frame was specifically designed to accommodate the brake. The challenge was to redesign the brake economically while maintaining its reliability and robustness. The original design proved to be very successful and operated flawlessly for fifteen years.

The redesigned eddy current brake is shown in figure 3-3 and can be compared with the original in figure 3-4. The new parts consist of the bearing housing and the support plate. The bearing housing both supports the bearings so that a preload can be applied, and also acts as a shaft that allows the assembly to rotate. The bearing housing is then bolted to

28

the support plate and the magnets and the return iron are then assembled to it. The motor support was reworked in order to accommodate the bearings. The assembly is then free to rotate about the motor support. The preload on the bearings can be adjusted by means of a shim plate between the bearing retainer and the motor support.

Two brackets that are mounted to rear side of support plate to restrain the brake, these brackets extend through the aft wall of the motor support. The brackets, as shown in figure 3-5, are attached to the motor support through two S-beam load cells.

The brake was first designed using only one load cell to restrain it. This proved to be a problem for the brake calibration. If only one load cell is used a reaction load must be transmitted through the bearings. The starting torque of the bearings is proportional to this reaction load. This starting torque resulted in hysterisis during the brake calibration. The addition of a second load cell reduced the reaction load on the bearings and the hysterisis problem. This is discussed further in the following section.

3.4 Torque Meter Calibration

Two approaches were used to calibrate the eddy current brake torque meter. Firstly, a static calibration performed on the brake using a precision torque sensor that mounted in series with the brake load cells. Secondly, a series of spin-down tests verified that brake performance was independent of the applied magnetic field.

3.4.1 Static Calibration

Calibration Setup

The torque meter is calibrated statically by applying a load to it through a precision torque sensor. The torque sensor is a commercial unit that has a calibration record traceable to NIST. The calibration setup is designed to minimize any bias errors that are introduced.

Figure 3-7 shows the mechanical setup for the calibration. The mounting plate shown in figure 3-7 transmits the calibration load from the torque sensor, through the brake assemble, to the load cells.

The design of this mounting plate ensures that the axis of the torque sensor is concentric with the axis of rotation of the brake. This important as any side loads applied to the torque sensor would place an additional torque to the brake (and therefore the load cells being calibrated) that would not be measured by the torque sensor. The resulting error would be the $\vec{\epsilon} \cdot \vec{F_s}$, where ϵ is the eccentricity, and F_s is the side load. The potential errors can be reduced by minimizing the both the eccentricity ϵ, and the side load F_s.

The calibration setup shown in figure 3-7 will introduce a side load on the torque sensor. This is a direct result of the way that the torque for the calibration is generated. The maximum error will occur if:

$$\vec{\epsilon} \cdot \vec{F_s} = \epsilon F_s \tag{3.5}$$

From figure 3-7 the side load can be estimated as:

$$F_s = \frac{T}{d} \frac{L_1}{L_2} \tag{3.6}$$

The bias introduced by the calibration setup can be estimated as:

$$\frac{B_T}{T} = \frac{\epsilon}{d} \frac{L_1}{L_2} \tag{3.7}$$

The maximum limit of the eccentricity ϵ, can be estimated by considering the design of the mounting plate. This plate is designed to ensure that the torque sensor is concentric and perpendicular with respect to the brake. A male alignment flange on the plate is inserted into the precision bearing-race. Another male alignment flange on the plate is aligned with the torque sensor. The alignment flanges are concentric to the plate to within 0.001 inches. The flanges were fit to their respective mates with clearances of less than 0.001 inches. The plate is bolted to return iron assemble using ten 0.25" bolts, through which the calibration load is transmitted.

A shaft extends from the torque sensor to the front of the main frame where the torque can be applied. A bearing, mounted to an I-beam spanning the mouth of the main frame,

30

supports the shaft. A lever arm is attached to the shaft in order to apply the torque. A 0.75-inch bolt, which is tightened through a nut welded to the I-beam, forces the lever arm and I-beam apart. This generates the required torque. A summary of the results is contained in table 3.2. A more complex calibration setup would have been required to eliminate the side load.

Another potential source of bias error in the calibration setup is the perpendicularity of the torque sensor with respect to the brake. This is a second order contribution, as the error will be proportional to the sine of the angle between the axis of the torque sensor and the brake. The load cells are calibrated for a maximum torque of 20,000 inch-pounds. This is a considerable load and it required the calibration hardware to pretty beefy.

Data Acquisition System

This section describes the data acquisition setup for the load cells and torque sensor used to calibrate them.

Precision strain gage amplifiers (Analog Devices 2B31) provide the excitation and amplify the output signal from the load cells. The amplifier gain and offset adjustment were replaced by precision resistors to ensure that the amplifier settings could not be adjusted. The idea being to calibrate the load cells and amplifiers as unit. The amplifier output was set to 0-4 volts to match the ± volts input to the data acquisition cards. The output range for the amplifier dropped to approximately 0-2 volts when the second load cell was added. The amplifiers were originally designed for use with only one load cell.

A voltmeter (Fluke Digital Multimeter 8520A) was used to record the output from the torque sensor. A 6-wire arrangement was used so that the bridge excitation could by measured at the connector provided by the manufacturer.

For the calibration, the data was recorded manually. The gain and offset for the calibration were determined by performing a linear least squares fit of the recorded data.

Static Calibration Results

This section discusses the results of the eddy current brake torque meter static calibration.

As discussed earlier the torque meter was originally designed using only one load cell. Figure 3-8 shows the results for calibration tests 5- 8. For each of the calibration runs, the deviation of the data points from the mean of the calibrations is plotted. Calibration tests 5 and 7 were performed as the torque was increased whereas for calibration 6 and 8 the torque was being reduced. The data shows a significant and consistent trend difference between the loading and unloading calibrations. The data shows a large discrepancy at low torque levels and more consistent results at higher torque levels.

If the starting friction of the bearings caused the problem, one would expect to see the opposite trend in the data. The torque measured should be lower than the applied torque (assuming that the average represents the actual torque). If there is a normal load on the bearing, the ball is depressed into the bearing race. For the ball to move it must effectively climb out of a depression that has been created by the normal load. In this case the normal load is caused by the reaction to the load cell. The slope of the starting friction versus normal load curve will decrease as the load is increased. The starting friction to torque ratio will be smaller at higher torque levels.

A description of other observations can help explain the data. As the torque is increased from one test point to the next, the torque level will slowly relax by approximately 0-5%. This takes about 20-30 seconds for the output voltages to stabilize so that a reading can be taken (three voltages must be recorded). If the torque is being decreased during the calibration the opposite trend in observed. The torque level will increase 0-5% until the reading stabilizes.

The torque is transmitted from the mounting plate through the return iron assembly and on to the load cells. The return iron is made up of a laminated transformer material that is held together by 10 quarter inch rods. This laminated material probably relaxes somewhat after the load has been increased. This can explain the observations seen above. Bearing starting friction can actually explain the irregularities in the test data. Because

Calibration Number	Scale $N \cdot m/Volt$	Zero $N \cdot m/Volt$	$\frac{dT}{dt}$	Mean $N \cdot m/Volt$	Deviation %
35	682.43	-17.07	+		
36	684.41	-26.17	-	683.42	-0.037%
37	682.18	-17.74	+		
38	684.74	-28.27	-	683.46	-0.031%
39	682.15	-17.30	+		
40	685.03	-29.76	-	683.59	-0.012%
41	682.82	-21.04	+		
42	684.52	-29.18	-	683.67	0.00%
43	682.17	-17.32	+		
44	685.81	-31.97	-	683.99	0.046%
45	683.45	-21.82	+		
46	684.36	-28.14	-	683.90	0.034%
Mean and Standard Deviation				863.67	0.034%

of the relaxation in the return iron, the torque is actually decreasing before the reading is taken, even though the torque is being increased from one data point to the next. The reverse trend is seen when the as the torque is reduced.

As the load is being increased, the torque is overestimated at low torque levels. The torque is underestimated at low torque levels as the load is reduced.

These problems can be attributed to the reaction on the bearings. To solve this problem a second load cell was added, the idea being to eliminate the reaction load on the bearings. However, adding a second load cell makes the system statically indeterminate, so the bearing load can be reduced, but it cannot be easily eliminated.

Figure 3-9 shows the calibration results with the second load cell added. The trend in the data is similar to the previous results, except that the magnitudes have been reduced. Table 3.2 contains data for two separate sets of calibration test that were performed 3 months apart. All of the calibration hardware was disassembled in between the two calibration tests. The calibration proved to be very repeatable.

The calibration results at the higher torque levels are excellent, they are repeatable to

within ±0.1%. However, the results are disappointing at low torque levels. During a typical blowdown test the torque measured at the brake will not be steady. A small imbalance in the rotor causes the brake to vibrate at the shaft frequency. Because of this vibration, the torque reading fluctuates by few percent about its mean value. The hysterisis seen in this static calibration should not have an affect on the torque measured in the real experiment. The torque reading will effectively jump back and fourth between the loading and unloading curves in figure 3-9. The result can be seen as a problem with the static calibration and not as an actual problem with the eddy current brake torque meter.

3.4.2   Spin-Down Calibration

This section describes the spin-down calibration. There are three objectives for the spin-down test. Firstly, to estimate the moment inertia of the rotating components. As shown in equation 3.1, the inertia is required to estimate the shaft power. The second objective of the test is to show that the repeatability the static calibration for high torque levels, is true for the all torque levels measured by the brake. Measuring the inertia at several different brake settings, and determining its repeatability, can do this. The final objective this test is to show that the strength of the magnetic field has no effect on the measurement.

This test was pretty straight froward, the experiment was setup as in the real blowdown experiment. The only difference being that the supply tank was not charged and the fast acting valve was not armed. Without the test gas, no power is generated so from equation 3.1 the rotor inertia can be estimated.

$$I = \frac{-T}{\frac{d\omega}{dt}} \tag{3.8}$$

Bearing friction was estimated from the rotor deceleration prior to the firing of the brake and was found to be negligible.

Three different brake settings were tested, table 3.3 contains the important parameters for the test. Figure 3-10 shows the unfiltered data for the torque measurement and figure 3-11 shows the rotor speed for the three runs.

34

Table 3.3: Torquemeter Spin-Down Calibration Summary

Calibration Number	Brake Excitation volts	Total Current amps	Rotor Speed rps	Measured Inertia $kg \cdot m^2$	Deviation %
1	133.7	254.0	100.16	1.8049	-0.20%
2	213.5	386.6	100.16	1.8095	0.06%
3	214.0	386.7	100.16	1.8086	0.01%
4	243.5	432.5	100.16	1.8109	0.13%
Mean and Standard Deviation				1.8085	0.13%

An FFT analysis of the of the torque signal showed peeks between 70-100 Hz, this is due to shaft vibration. A 5 pole Butterworth filter with a cutoff at 50Hz, and phase shifting was applied to smooth the raw data.

Equation 3.8 requires that the derivative of the speed signal be taken. This is not practical, as differentiation will amplify the noise in the already noisy signal. Instead a linear least squares curve was fit to the data and its derivative was taken to get the angular deceleration. The curve was fit to 80 milliseconds segments of data, the torque is taken as the mean torque over the same range. Figure 3-12 shows the calculated inertia for the four tests. The inertia is plotted as a function of the torque level at which it is estimated. The data shows that the calculated inertia is constant over the entire range of tested.

Figure 3-13 shows the deviation from the mean torque over the entire range. The mean inertia is $1.8085kg \cdot m^2$ and the standard deviation is 0.13%.

3.4.3 Uncertainty Analysis

The bias estimate for the torque measurement was determined by combining the quoted uncertainty for the torque sensor (0.05%) and the precision index for the static calibration (from Table 3.2). This gives a bias limit of 0.084%. The precision index for the torque measurement is taken from the spin-down calibration (Table 3.2). The combined 95% uncertainty level is 0.27%.

3.5 Summary

A static calibration has been performed to determine the scale for the eddy current brake. At high torque levels the measurement are very repeatable. The result was less conclusive at lower torque levels. The mean of the scales for the loading and unloading of each calibration cycle repeats with a standard deviation of 0.034%.

A spin-down test was performed to estimate the inertia of the rotating components. This calibration showed that the inertia measurement repeated with a standard deviation of 0.13% over the entire torque range of interest. This shows that the scale determined from the static calibration at the high torque levels is valid over the entire range of operation of the brake. The spin-down test also verified that the brake current does not adversely affect the torque measurement. The estimated uncertainty (U_{95}) for the eddy current brake torque measurement is 0.27%.
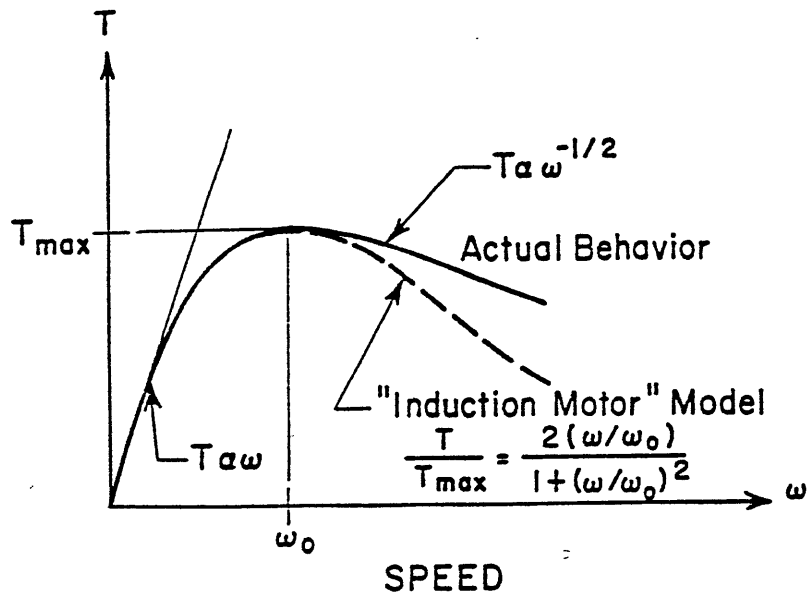
Figure 3-1: Eddy Current Brake Torque vs Rotational Speed

A - ISOLATION AMPLIFIERS (AD 289J)
S - VACUUM CONTACTOR (ITT RP 900K)
V - VARISTOR (GE VS II 8A60)
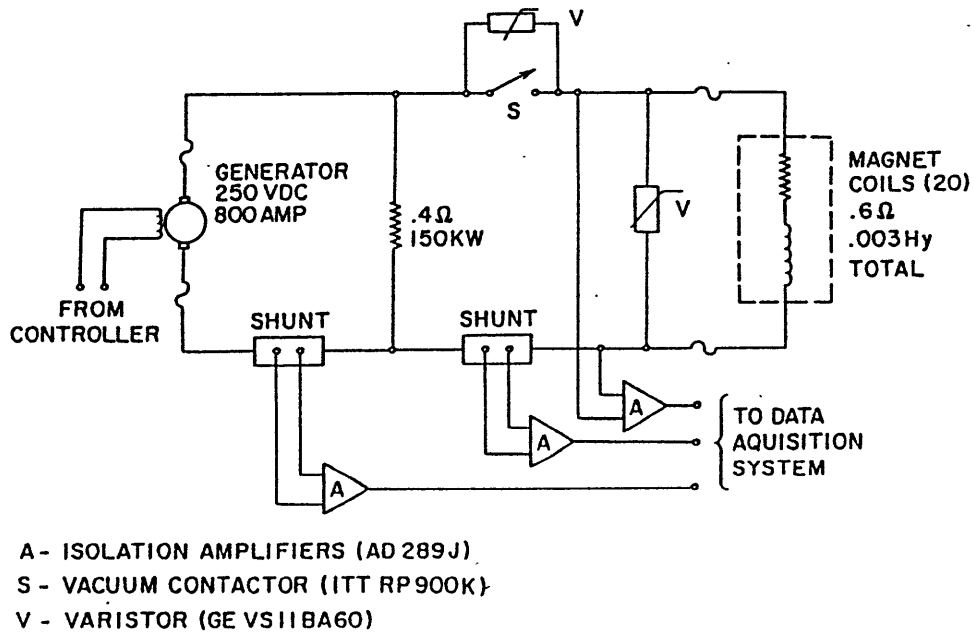
Figure 3-2: Brake Magnet Current Switching Circuit
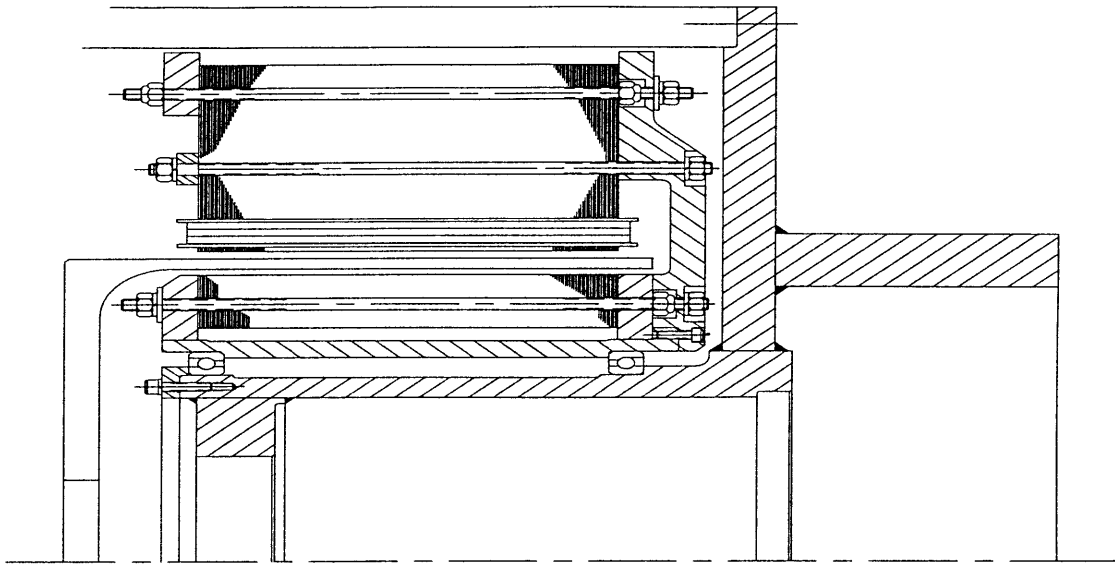
Figure 3-3: Redesigned Eddy Current Brake
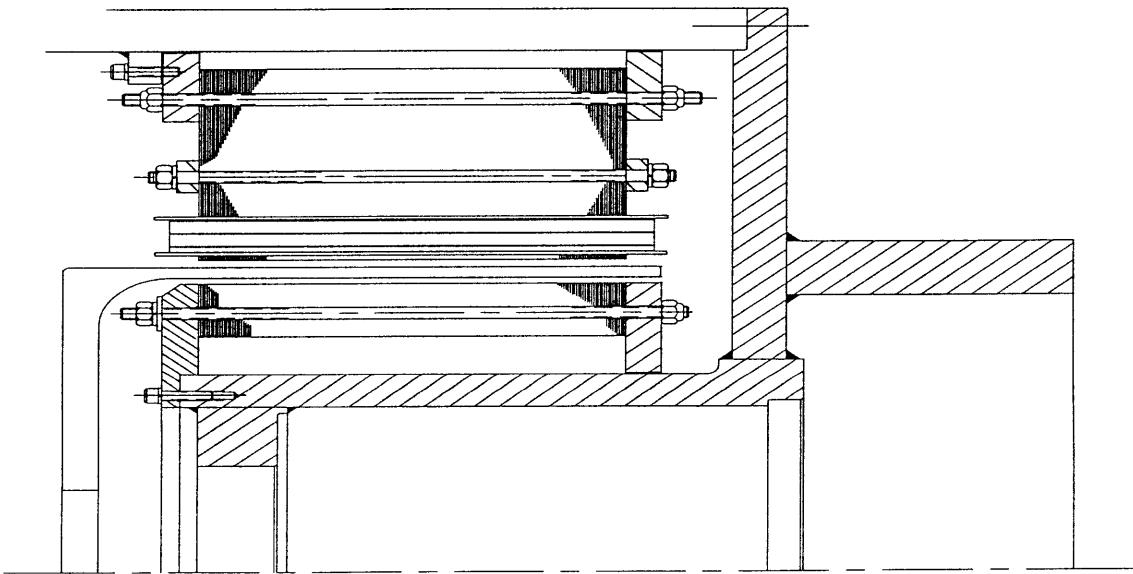
Figure 3-4: Old Eddy Current Brake
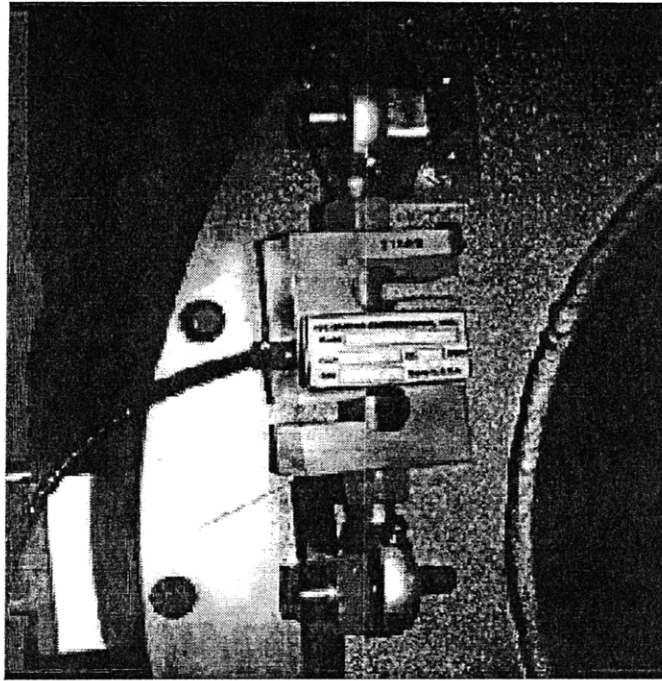
Figure 3-5: Eddy Current Brake Load Cell, (one of two)
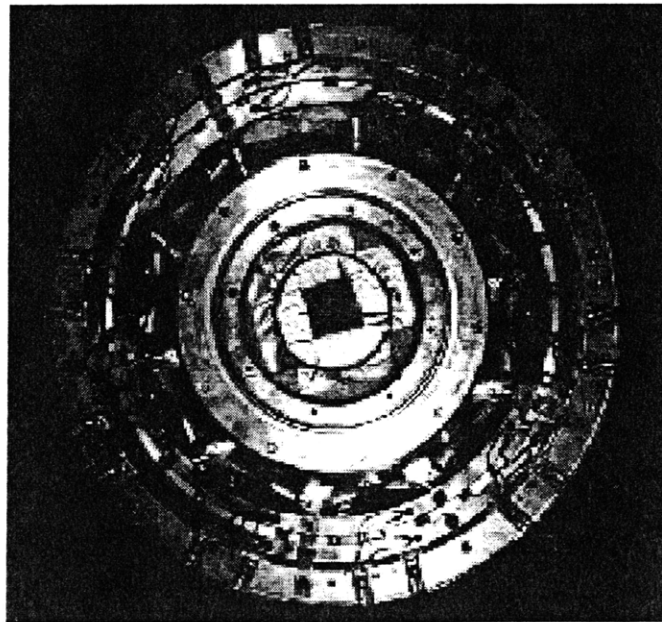
Figure 3-6: Redesigned Eddy Current Brake
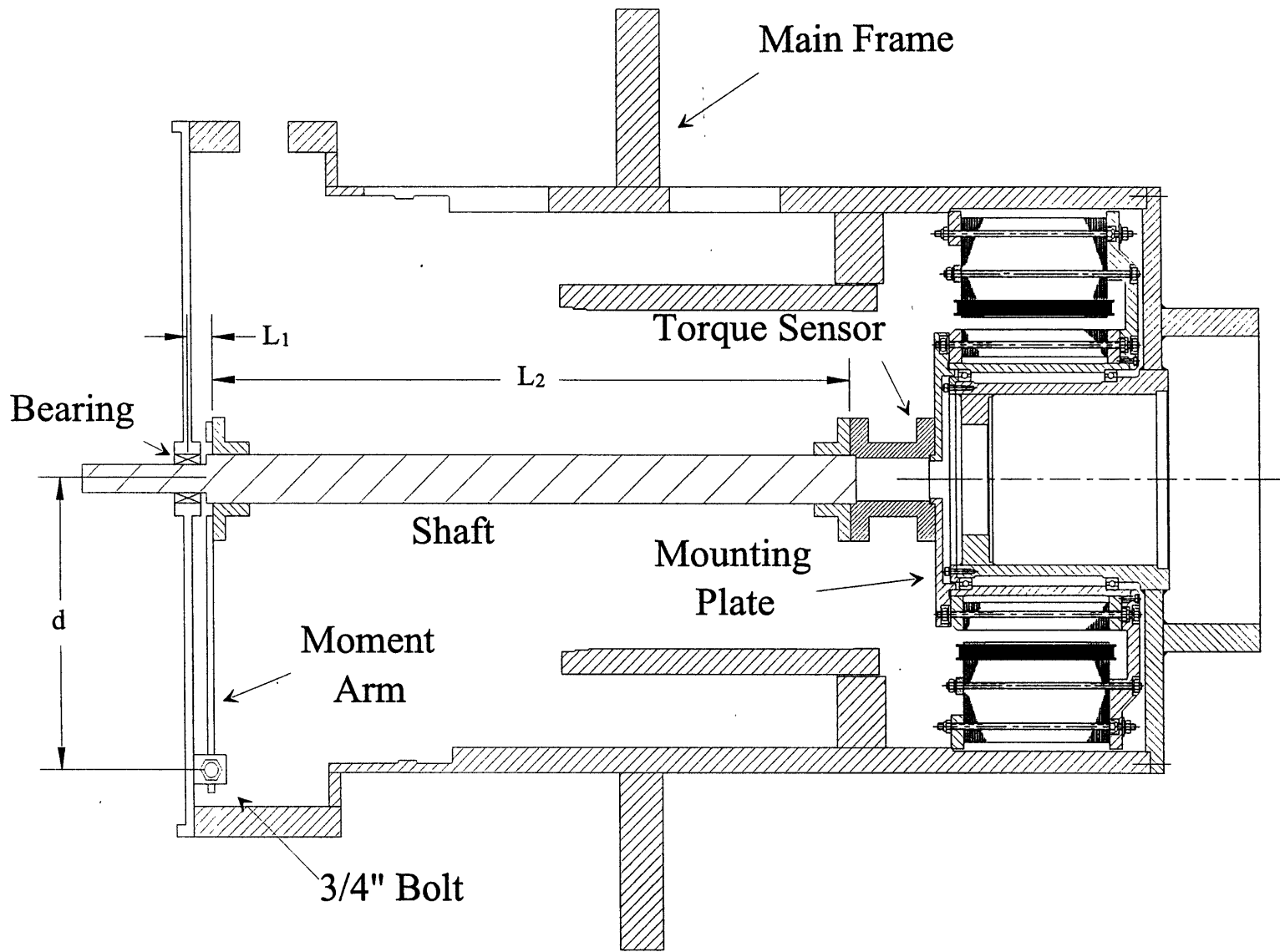
Figure 3-7: Static Calibration Setup

40
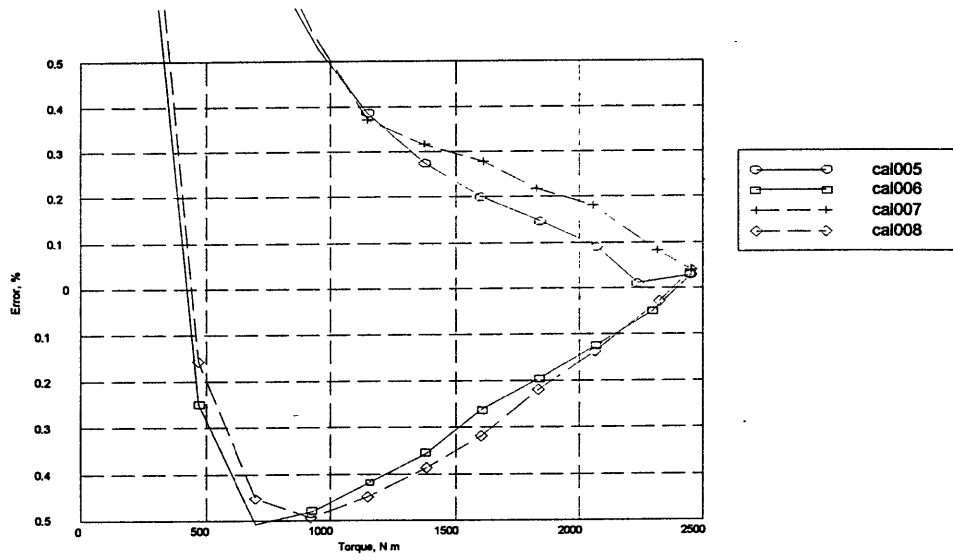
Figure 3-8: Static Calibration, one load cell
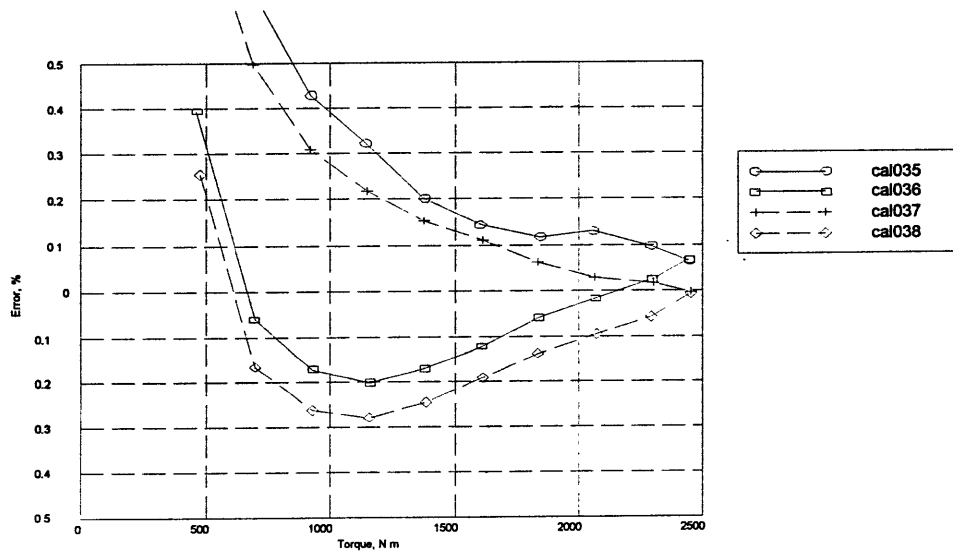
Figure 3-9: Static Calibration, two load cell

41
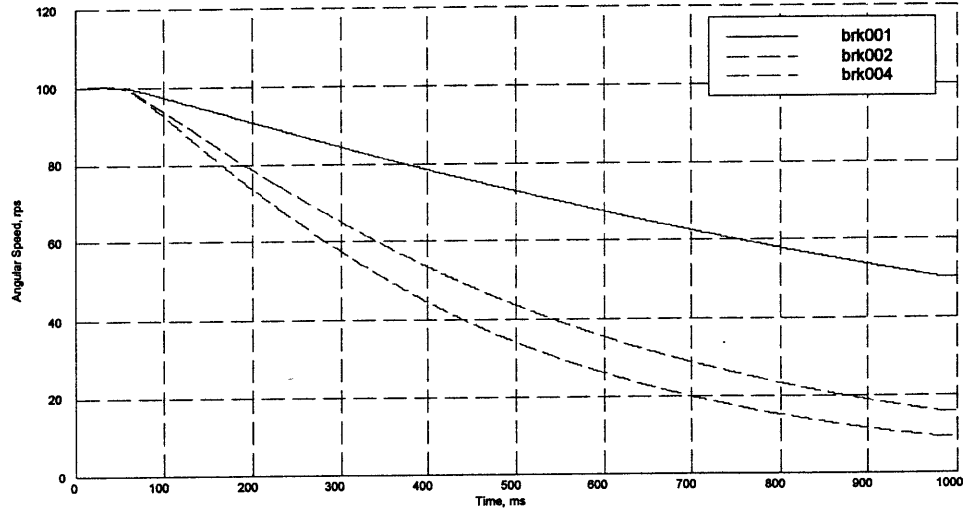
Figure 3-10: Spin-Down Tests, Rotational Speed
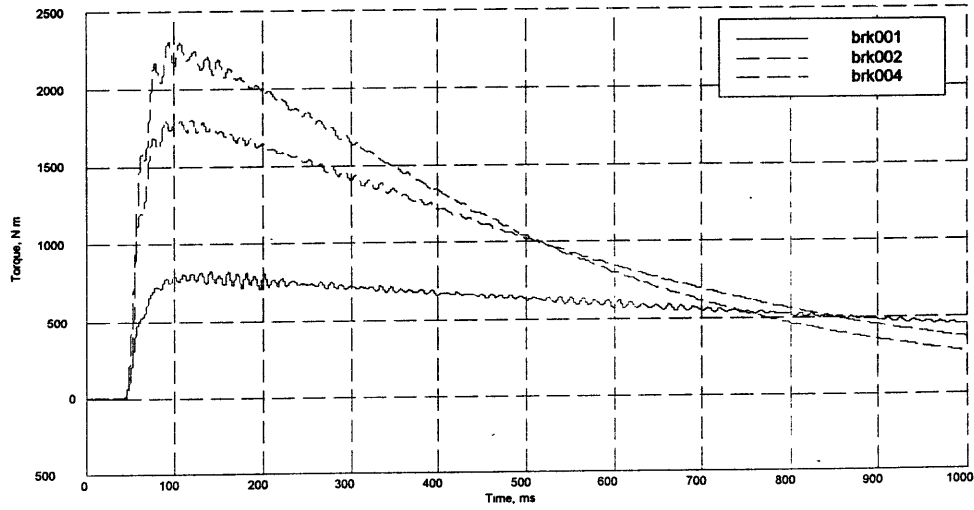
Figure 3-11: Spin-Down Tests, ECB Torque

42
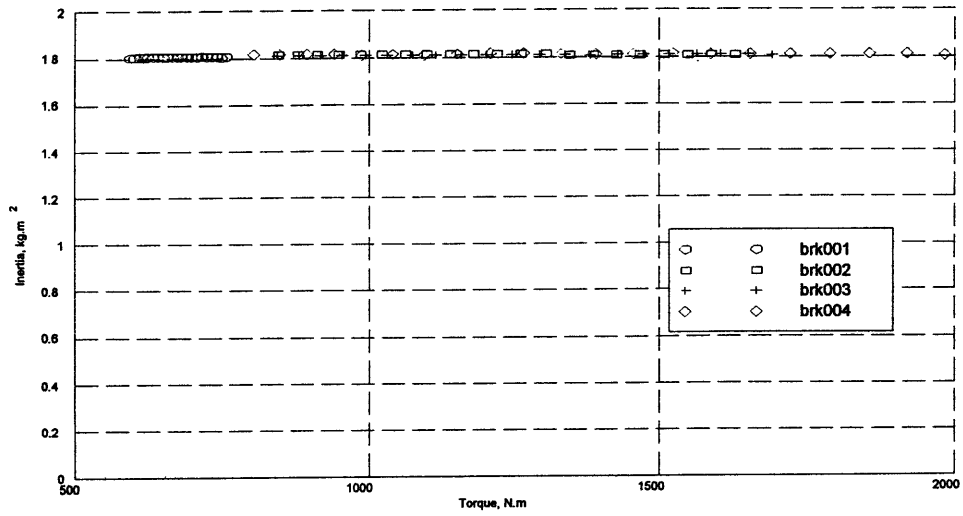
Figure 3-12: Spin-Down Tests, Calculated Inertia vs Torque
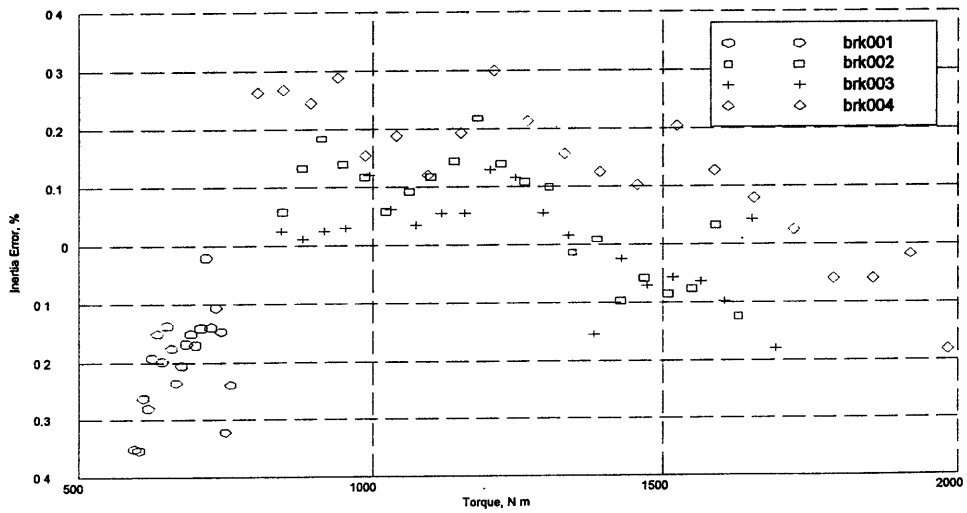
Figure 3-13: Spin-Down Tests, Inertia Error vs Torque

43

Chapter 4

Mass Flow Measurement

4.1 Introduction

Accurate turbine mass flow measurement is required in order to evaluate stage shaft efficiency and turbine capacity. In this study a critical flow venturi is used to measure the turbine mass flow. This method was chosen, as it is an industry standard for measuring large volumetric flow rates[7]. A nationally recognized laboratory calibrated the discharge coefficient of the nozzle with tractability to the National Institute for Standards and Technology. The calibrated venturi is used as a transfer standard for the measurement of mass flow in the blowdown turbine facility. A well-established method for dealing with the real gas behavior of test gases is another benefit of the critical flow venturi.

Sections 4.2, 4.3, and 4.4 review the ANSI standard [10] for mass flow measurement, and how it was applied to the blowdown turbine facility. Section 4.5 outlines a correction that must be applied to the measured flow rate to account for the transient effects of the short duration test. Section 4.6 reviews the error analysis for the mass flow measurement and the transient correction.

4.2 The Sonic Nozzle Standard

A sonic nozzle is a venturi nozzle through which the mass flow rate is the maximum possible for given upstream conditions. At critical flow or choked conditions, the average gas velocity at the nozzle throat is the local sonic velocity. A sonic nozzle was chosen as a mass flow meter because of its well defined fluid dynamic characteristics. Because of its smooth convergent divergent section the discharge coefficient of the venturi nozzle is known to be very lose to unity. If the nozzle geometry and installation conform to ANSI standard [10], the calculated discharge coefficient will have a stated uncertainty of $\pm - 0.5\%$. This uncertainty can be reduced to about $\pm - 0.25\%$ by calibrating the nozzle against a calibration laboratory primary standard.

This second option was chosen for two reasons, firstly, the maximum accuracy was desired, and secondly, the upstream duct requirement of the standard would not be practical for the MIT Blowdown turbine facility. If placed downstream of the turbine, 20 feet of straight ducting would be required to satisfy the standard. Colorado Engineering Experiment Inc. (CEESI) calibrated the nozzle with the upstream duct and flow conditioning as shown in figure 4-5.

4.3 Basic Equations

Ideal critical flow rates require three main conditions: (a) the flow is one-dimensional; (b) the flow is isentropic; and (c) the gas is perfect. Under these conditions, the value of critical flow rate is:

$$\dot{m} = A\,C_{*i}\,\frac{P_0}{\sqrt{R\,T_0}} \tag{4.1}$$

where

$$C_{*i} = \sqrt{\gamma \left(\frac{2}{\gamma+1}\right)^{\left(\frac{\gamma+1}{\gamma-1}\right)}} \tag{4.2}$$

45

4.3.1 Flow Rate in Real Conditions

Discharge Coefficient

However, the real gas flow rate will differ in two respects, firstly the flow is not quite one dimensional. Blockage due to boundary layer growth along the walls of the nozzle will reduce the mass flow. Also, there is a small static pressure non-uniformity at the throat of the nozzle due to streamline curvature effects. To account for the multi-dimensional nature of the flow, A in equation 4.1 is replaced by AC_d, were C_d is discharge coefficient of the nozzle. Secondly, the test gas is not quite perfect and real gas thermodynamic effects must be considered. To account for real gas effects C_i in equation 4.1 is replaced by C_R. These changes yield equation 4.3:

$$\dot{m} = A\,C_d\,C_R\,\frac{P_0}{\sqrt{R\,T_0}} \tag{4.3}$$

The nozzle was calibrated at an independent, nationally recognized laboratory that specializes in the calibration of critical flow venturi nozzles for the natural gas and aerospace industries. The calibration is tracible to the National Institute of Science and Technology. The nozzle discharge coefficient is dependent on Reynolds number and is generally expressed in the form:

$$C_d = a - b\,Re_d^{-n} \tag{4.4}$$

Where a,b, and n are obtained by calibration. Table 4.1 contains the calibration results for the nozzle. Reference [14] contains a boundary layer calculation of nozzle discharge coefficient, the results are also shown in table 4.1 for comparison. Many investigators favor this type of nozzle design because of the close agreement between the experimental and the theoretical results.

Figure 2-1 shows the installation of the nozzle in the blowdown turbine facility. The flowfield upstream of the nozzle is not the ideal flowfield that is called for in the ANSI standard. The flow exits the turbine in an annulus and the recombines downstream of the

Table 4.1: Nozzle Discharge Coefficients

Parameter	ANSI Standard	MIT Nozzle
a	0.9885	0.9832
b	0.445	12.978
n	-0.5	-0.5
C_d at $Re = 6 \cdot 10^6$	0.9929	0.9885

starter motor to a cylindrical cross section. This will result in a significant blockage at the flow centerline. The flow conditioning upstream if the nozzle will reduce the non-uniformity before it enters the nozzle.

In order to determine the sensitivity of the nozzle to the upstream blockage, the nozzle was calibrated with and without a simulated upstream blockage in place. Figure 4-1 shows that the effect of the blockage is not significant, fiqure 4-5 shows the nozzle location relative to the simulated blockage.

Critical Flow Coefficient

When critical flow nozzles meter gasses, errors frequently arise when conventional one-dimensional isentropic flow relations are used to compute the mass flow rate. The assumption usually made is that the gas is ideal. The ideal gas being defined as one that a constant specific heat capacity and a compressibility factor of unity. In many engineering applications these are valid assumptions. However, CO_2, the test gas being used in this experiment exhibits significant non- ideal behavior in the range of pressures and temperatures under which the nozzle operates. The difference between C_i and C_R under typical test conditions for this application is 1.0%. This would be a significant source of error if unaccounted for.

In order to estimate C_R, the pressure-density-temperature and the differential enthalpy and entropy relations must be examined.

The pressure-density-pemperature relation is given by equation 4.5:

$$Z = \frac{P}{\rho R T} = Z\left(\rho, T\right) \tag{4.5}$$

47

Alternatively Z can be expressed as a function of density and temperature.

The experssions for the differential entropy and enthalpy are:

$$dS = C_p \frac{dT}{T} + \frac{1}{\rho^2} \left(\frac{\delta \rho}{\delta T} \right)_p dP \qquad (4.6)$$

$$dH = T \, dS + \frac{1}{\rho} dP \qquad (4.7)$$

Since it is assumed that the flow is isentropic:

$$dS = 0 \qquad (4.8)$$

And from the relation:

$$dH = -V \, dV \qquad (4.9)$$

Substituting equations 4.5, 4.8, and 4.9 into 4.6 and 4.7 yields the result:

$$\frac{dS}{R} = \frac{C_p}{R} \frac{dT}{T} - \left[Z + T \left(\frac{\delta Z}{\delta T} \right)_P \right] \frac{dP}{P} = 0 \qquad (4.10)$$

$$-\frac{V \, dV}{R} = \frac{C_p}{R} dT - T^2 \left(\frac{\delta Z}{\delta T} \right)_P \frac{dP}{P} \qquad (4.11)$$

Equations 4.10 and 4.11 are integrated along the path indicated in figure 4-2.

The pressure end point of the path is P_1 satisfies the integral of equation 4.10; that is $S_1 = S_0$. At this point, equation 4.11 can be integrated along the same path. The result of this integration permits the evaluation of the nozzle throat velocity V_1. The speed of sound in the nozzle throat can then be evaluated from the expression:

$$\frac{1}{a^2} = \left(\frac{\delta \rho}{\delta P} \right)_S = \left(\frac{\delta \rho}{\delta P} \right)_T + \left(\frac{\delta \rho}{\delta T} \right)_P \left(\frac{\delta T}{\delta P} \right)_S \qquad (4.12)$$

Where $\left(\frac{\delta \rho}{\delta P} \right)_T$ and $\left(\frac{\delta \rho}{\delta T} \right)_P$ are derived from the state equation 4.5, and $\left(\frac{\delta T}{\delta P} \right)_S$ is derived

from the integrated form of equation 4.11. The nozzle throat Mach number is then given by:

$$M' = \frac{V_1}{a_1} \tag{4.13}$$

Since the Mach number in general will not be unity, a new throat temperature is estimated. The temperature correction to be added to previous temperature estimate is:

$$\Delta T = \left[\left(\frac{\delta T}{\delta M}\right)_S\right]_i \Delta M \tag{4.14}$$

Where $\left[\left(\frac{\delta T}{\delta M}\right)_S\right]_i$ is estimated from the isentropic ideal-gas relation, and ΔM is the difference between the desired and calculated Mach number. This process is repeated until ΔM is less than 10^{-5}. At this point the state and the velocity of the gas at the nozzle throat are considered known. The real gas critical flow coefficient is then defined as:

$$C_R = \frac{P_1}{P_0} \frac{\sqrt{T_0}}{Z_1 T_1} \sqrt{\frac{V_1{}^2}{R}} \tag{4.15}$$

Two different methods were used to determine C_R. Firstly the above method was implemented using Johnson's [12] algorithm. The equation of state for CO_2 was taken from [18]. As a second check, NIST14 [15] was modified to calculate C_R. NIST14 is a code developed by the National Institute for Standards and Technology that generates the thermophysical properties of gas mixtures. The code accounts for the real gas interaction between the test mixtures. Both of these methods gave the same result for C_R. The ANSI standard [10] gives sample values for C_R for different gases, these not recommended values and are intended as general information on the magnitude and variation of C_R. The values calculated agreed with the ANSI standard [10] within ±0.1%.

4.4 Nozzle Design and Installation

The critical flow venturi nozzle was designed to closely match the ANSI standard [10] toroidal throat nozzle. However, because of the design constraints of modifying an existing facility, some of requirements of the standard could not be satisfied. For this reason it was decided to have the nozzle calibrated at an independent laboratory that specializes in calibrating critical flow venturi nozzles. This approach also offered the opportunity to reduce the estimated uncertainty for the nozzle discharge coefficient.

Two common nozzle designs are controlled by reference [10] standard, firstly the toroidal throat venturi nozzle and secondly the cylindrical throat nozzle. The main difference between the two that the latter has a cylindrical section between the throat and the exit cone, whereas the toroidal throat nozzle transitions directly from the inlet contour to a divergent cone, as shown in figure 4-6. Discharge coefficients for the toroidal throat nozzle design may be determined by theoretical calculation. The coefficients so obtained agree well with experimental data [14]. Because of the relative ease of calculation of the theoretical coefficient and its agreement with experimental data, some investigators favor this design over the cylindrical throat design [10].

The following sections will paraphrase the design requirements for standard toroidal throat venturi nozzle and compare how the MIT blowdown turbine nozzle differs.

From the ANSI standard [10].

5.2 General Requirements

5.1.1 The venturi nozzle shall be inspected to determine conformance to this Standard.

5.1.2 The venturi nozzle shall be manufactured from a material suitable for its intended application. The following are some considerations.

(a) The material should be capable of being finished to the required condition. Some materials are unsuitable because of pits, voids, and other non-homogenates.

(b) The material, together with any surface treatment used, shall not be subjected to corrosion in the intended service.

(c) The material should be dimensionally stable and should have known and repeatable

thermal expansion characteristics (if it is to be used at a temperature other than that at which the throat diameter has been measured), so that an appropriate throat diameter correction can be made.

5.1.3 The throat and toroidal inlet up to the conical divergent section of the venturi nozzle shall be smoothly finished so that the arithmetic average roughness height does not exceed $15 \times 10^{-6}d$.

5.1.4 The throat and toroidal inlet up to the conical divergent section shall be free from dirt, films, or other contamination.

5.1.5 The form of the conical divergent portion of the venturi nozzle shall be controlled such that any steps, discontinuities, irregularities, and lack of concentricity shall not exceed 1pc of the local diameter. The arithmetic average roughness of the conical divergent section shall not exceed 10^{-4} d.

5.2 Standard Venturi Nozzles

5.2.1 Toroidal Throat Venturi Nozzle

5.2.1.1 The venturi nozzle shall conform to figure (see [10]).

5.2.1.2 For the purposes of locating other elements of the venturi nozzle critical flow metering system, the inlet plane of the venturi nozzle shall be defined as that plane perpendicular to the axis of symmetry which intersects the inlet at a diameter equal to $2.5d \pm 0.1d$.

5.2.1.3 The convergent part of the venturi nozzle (inlet) shall be a portion of the torus that shall extend through the minimum area section (throat) and shall be tangent to the divergent section. The contour of the inlet upstream of a diameter equal to $2.5d$ is not specified, except that the surface at each axial location shall have a diameter equal to or greater than the extension of the toroidal contour.

5.2.1.4 The inlet toroidal surface of the venturi nozzle beginning at a diameter of 2.5d perpendicular to the axis of symmetry and extending to the point of tangency shall not deviate form the shape of a torus by more than $\pm 0.001d$. The radius of curvature of the toroidal surface in the plane of symmetry shall be $1.8d$ to $2.2d$.

5.2.1.5 The divergent portion of the venturi nozzle shall form a frustrum of a cone with a half-angle of 2.5° To 6°. The length of the conical section shall not be less than the throat

diameter.

6 Installation Requirements

6.1 General

This standard covers installation when either: (a) the pipeline upstream of the nozzle is of circular cross section; or (b) it can be assumed that there is a large space upstream of the venturi nozzle. For case (a), the primary device shall be installed in a system meeting the requirements of para. 6.2. For case (b), the primary device shall be installed in a system meeting the requirements of para. 6.3. In both cases swirl must not exist upstream of the venturi nozzle. Where a pipeline exists upstream of the nozzle, swirl-free conditions can be ensured by installing a flow straightener of the design in figure (see [10]) at a distance greater than 5D upstream of the nozzle inlet plane.

6.2 Upstream Pipeline

The primary device may be installed in a straight circular conduit, which shall be concentric within 0.02D with the centerline of the venturi nozzle. The inlet conduit up to 3D upstream of the venturi nozzle shall not deviate form circularity by more than 0.01D and shall have an arithmetic average roughness height which shall not exceed $10^{-4}D$. In order to meet the coefficient specifications of this Standard the diameter of the inlet conduit shall be a minimum of $4d$. It should be noted that the use of β ratios larger than 0.25 increases the effect of upstream disturbances, and moreover, makes corrections necessary t the measured pressure and temperature.

MIT Venturi Nozzle

The nozzle was manufactured from Stainless Steel 304 and designed to meet the general requirements 5.1.1 to 5.1.5. The inlet contour does not meet requirements 5.2.1.3 and 5.2.1.4 of the standard. For ease of manufacrure the inlet contour transitions from a toroidal to a conical section at approximately $1d$ from the inlet plane. The divergent portion meets requirement 5.2.1.5.

MIT Nozzle Installation The nozzle installation is shown in figure 4-5. The upstream pipeline meets the requirements in 6.2 except; (a) the duct extends 2.5D upstream of the nozzle not 3D, (b) a β ration of 0.385 was used rather than the 0.25 recommended in the

standard.

4.5 Transient Correction

4.5.1 Introduction

Critical flow venturi nozzles are intended for steady flow applications. For this application the flow is steady with respect to the time scales of the flow through the nozzle, as it is for the turbine stage itself. However, as this is a transient test, the conditions upstream of the nozzle will change somewhat over the duration of the test. As the temperatures and pressures change in the volumes connecting the turbine and the venturi nozzle, this will introduce a capacitive effect where mass is stored. The mass flow rate through the nozzle may not match that through the turbine at a given time. An estimate must be made of this effect, as if it is unaccounted for it could constitute a significant error source. The relationship between the turbine and nozzle mass flows can be described by equation 4.16.

$$\dot{m}_{Turbine} = \dot{m}_{Nozzle} + \dot{m}_{Stored} \tag{4.16}$$

The mass flow due to storage can be estimated by manipulating the state equation as follows:

$$PV = mRZT \tag{4.17}$$

$$m = \left(\frac{P}{T}\right) \frac{V}{RZ} \tag{4.18}$$

And then taking its derivative with respect to time:

$$\dot{m} = \frac{V}{RZ} \left(\frac{1}{T}\right) \frac{dP}{dt} - \frac{V}{RZ} \left(\frac{P}{T^2}\right) \frac{dT}{dt} \tag{4.19}$$

Section 4.5.4 will outline how the pressure and temperature dependent terms in eqation 4.19 are either measured or approximated.

4.5.2 Compressional Heating

Compressional heating is an interesting phenomenon observed in transient testing that is not seen in steady state test rigs. When a throttling process (flow through a valve) is followed by an isentropic compression (chamber filling from vacuum), the temperature of the gas in the filled compartment can exceed the initial temperature of the gas. This is seen in the MIT Blowdown Turbine facility during the start up transients of the test. In the past this phenomenon was a merely a novelty that was interesting to note on the fast response thermocouples.

Compressional heating is significantly more important to the current task of estimating the transient correction to the mass flow measurement. The gas that is heated is convected through the primary flow path in 0-100ms and does not affect the transient correction for the primary flow path. However, there also exists a secondary flow path in parallel with the primary, as shown in figure 4-7. The time scale for the flow through the secondary flow paths is significantly longer. The temperatures in the secondary compartments will be higher than the primary flow path, because of compressional heating. The compartment temperatures are required to estimate $\dot{m}_{Stored}$, as shown in equation 4.16.

The increase in temperature due to compressional heating for a simple compartment filled through an orifice, from a constant temperature reservoir, can be estimated as follows:

For isentropic compression a compartment, pressure in related to its volume by:

$$VP^{\frac{1}{\gamma}} = k \tag{4.20}$$

or,

$$V = P^{-\frac{1}{\gamma}}k \tag{4.21}$$

The fractional change in volume with pressure is:

$$dV = -\frac{1}{\gamma}P^{-\frac{1+\gamma}{\gamma}}kdP \tag{4.22}$$

The fractional change in mass can then be estimated using the state equation:

$$dm = \rho dV = \frac{P}{RT_0} \left(-\frac{1}{\gamma} P^{-\frac{1+\gamma}{\gamma}} \right) \left(P^{\frac{1}{\gamma}} V \right) dP = -\frac{1}{\gamma} \frac{V}{RT_0} dP \qquad (4.23)$$

The total mass in the compartment can be found by integrating dm over the pressure range from vacuum to the supply pressure:

$$m = \int_0^{P_0} -\frac{1}{\gamma} \frac{V}{RT_0} dP = -\frac{1}{\gamma} \frac{V P_0}{RT_0} \qquad (4.24)$$

The final compartment temperature can calculated from the mass, the final pressure, and the state equation:

$$T = \frac{P_0 V}{Rm} = \frac{P_0 V}{R \left(-\frac{1}{\gamma} \frac{P_0 V}{RT_0} \right)} = \gamma T_0 \qquad (4.25)$$

This is an important result as it shows that the final compartment temperature is only a function of the supply temperature and γ. Compressional heating is an important concept and will be referred to in the following sections.

4.5.3   The Model

A fairly detailed mathematical model of the blowdown dynamics of the facility was constructed for the conceptual design of this experiment. Also, to determine if the correction in equation 4.16 could be made, and with what level of confidence.

Adding another choke point in the flow path significantly affects the dynamics of the system. It was difficult to design a nozzle that was feasible to manufacture, and would remain choked for the duration of the test, and while still maintaining choked flow at the throttle plate downstream of the turbine. It is necessary to maintain choked flow across the throttle plate in order to keep the pressure ratio across the turbine stage constant. Also, it is necessary to maintain choked flow across the venturi nozzle, otherwise it wouldn't be a critical flow venturi.

In order to extend the useful test time a extended diffuser is added downstream of the

Table 4.2: Compartment Volumes

Compartment	V_0	V_1	V_2	V_3	V_4	V_5	V_6	V_7	V_8
Volume	364.0	5.0	1.45	23.43	21.45	523.0	0.485	0.619	1.320
Volume Bias Limit, %	-	-	2%	1%	1%	-	5%	1%	20%

nozzle. The area ratio of the diffuser is 1:2, this allowed a maximum permissible back pressure ratio of 0.87. For the nozzle throat to exit area ratio, and γ this is the maximum pressure ratio that the reference [10] recommends without verifying that the nozzle remains choked.

The model inputs include; compartment connections, connection areas, and compartment volumes. The model assumes one-dimensional adiabatic flow between the volumes, where a simple throttling process was assumed between each compartment. At each iteration the compartment pressures determine the mass flow magnitude and direction. The compartment pressures are then updated based on changes in the internal energy of each compartment. A simple backward Euler iteration scheme was used.

Tables 4.2 and 4.3 contains sample input data for the model. Figure 4-7 shows a schematic of the model of the blowdown turbine facility. The transient mass flow correction is driven primarily by volumes 3 and 4. These represent the dump tank extension duct and the nozzle upstream plenum. The size of volume 3 is driven by the need to relocate the eddy current brake and the starter motor out of the dump tank. The size of volume 4 is set by the need to provide an adequate length of ducting upstream of the nozzle. Volumes 3 and 4 are the dominant source of the correction and their magnitude can be estimated with a high degree of confidence. Volumes 2, 6, and 7 can be estimated easily also (2 and 6, with the aid of a 3D solid modeling program). Volume 8 houses the eddy current brake and is more difficult to accurately measure.

Table 4.3: Compartment Areas

Compartment	A_{01}	A_{12}	A_{23}	A_{34}	A_{45}	A_{15}	A_{26}	A_{67}	A_{78}	A_{83}
Area	-	22.0	42.0	150.0	78.0	10.62	1.20	1.10	2.52	2.51

4.5.4 Mass Flow Correction

In estimating the mass flow due to storage volumes 6, 7, and 8 will be considered separately form volumes 2, 3, and 4. Volumes 2, 3, and 4 constitute the main flow path between the turbine and the nozzle. Volumes 6, 7, and 8 are secondary compartments that cannot be feasibly be sealed and must also be considered.

The compartment pressures and temperatures for the primary flow path are measured directly. Compartments 2 and 4 are already instrumented to determine the turbine exit conditions and the conditions upstream of the critical flow venturi respectively. Total pressure and temperature probes were installed in compartment 3 also.

For the secondary compartments the pressures and temperatures are a little more difficult to determine. The temperatures are very difficult to measure, both because of their location and because significant temperature gradients may exist within the compartments. The model is used to determine if any simplifying assumptions can be made about the conditions in these compartments.

Figures 4-8 and 4-9 show the predicted pressure and temperature histories during the experiment. In the secondary compartments, the temperature initially rise because of compressional heating as discussed in section 4.5.2, and then falls as the hot gas is convected downstream. The pressures in the secondary flow path are primarily a function of the secondary mass flow and areas connecting the compartments. Both the pressures and temperatures in the secondary compartments are strongly dependent on areas connecting the compartments. The discharge coefficients for these areas are not known, and their effect can only be estimated by considering reasonable values to bound their influence.

In order to simplify the task of making this correction another approach was considered. Area A_{67} is used to provide an access for instrumentation, and can be sealed without too

much effort. This modification eliminates the secondary flow path that bypasses the main flow. Instead, the secondary compartments empty into the main flow path compartments from which they are filled.

Figures 4-10 and 4-11 show the predicted pressure and temperature histories with this modification. For the correction V_7 and V_8 are simply lumped in with V_3, and V_6 is added to V_2. From figures 4-10 and 4-11 this is clearly reasonable. Figure 4-12 shows the mass flow through the turbine and nozzle. Figure 4-13 shows the error in mass flow, or the magnitude of the correction required to estimate $\dot{m}_{Turbine}$ from $\dot{m}_{Stored}$ and $\dot{m}_{Nozzle}$. Figure 4-13 also shows the error in mass flow using this same simplification, without the modification to the facility.

The window in the test where the correction to the mass flow can be made is approximately be made is between 350 to 800 ms. Below 350 ms the correction is too large, and above 800ms the nozzle may not be choked. At 500ms $\dot{m}_{Stored}$ is zero, the turbine mass flow equals the nozzle mass flow. As can be seen from figure 4-10, the slope of the pressure curve is approximately zero.

In summary, a simple one-dimensional model of the blowdown turbine facility has been used to show that the difference between $\dot{m}_{Turbine}$ and $\dot{m}_{Nozzle}$ over the range of interest is on the order of +/- 4%. The magnitude of the correction can be estimated from pressure and temperature measurements between the nozzle and turbine. A minor change to the facility will reduce the uncertainty of this correction.

4.6   Mass Flow Measurement Error Analysis

The precision index for the mass flow measurement can be estimated from:

$$S_{\dot{m}} = \sqrt{\left(\frac{\delta \dot{m}}{\delta C_d} \cdot S_{C_d}\right)^2 + \left(\frac{\delta \dot{m}}{\delta C_R} \cdot S_{C_R}\right)^2 + \left(\frac{\delta \dot{m}}{\delta P_0} \cdot S_{P_0}\right)^2 + \left(\frac{\delta \dot{m}}{\delta T_0} \cdot S_{T_0}\right)^2} \qquad (4.26)$$

If we define the influence coefficient for each variable in equation 4.26 as:

$$C_* = \frac{\delta \dot{m}}{\delta *} \cdot \frac{*}{\dot{m}} \qquad (4.27)$$

Then equation 4.26 can be rewritten as:

$$\frac{S_{\dot{m}}}{\dot{m}} = \sqrt{\left(C_{C_d} \cdot \frac{S_{C_d}}{C_d}\right)^2 + \left(C_{C_R} \cdot \frac{S_{C_R}}{C_R}\right)^2 + \left(C_{P_0} \cdot \frac{S_{P_0}}{P_0}\right)^2 + \left(C_{T_0} \cdot \frac{S_{T_0}}{T_0}\right)^2} \qquad (4.28)$$

This is a more useful form than that of equation 4.26. The influence coefficient is a non-dimensional parameter that represents the how a given error source will be propagate to overall measurement error. The influence coefficient represents the relative amplification of that source error through equation 5.3. The sign of the influence coefficient is not important as the term is squared. The influence coefficients C_{C_d}, C_{P_0} and C_{T_0} are straightforward:

$$C_{C_R} = 1, C_{C_d} = 1, C_{P_0} = 1, C_{T_0} = -\frac{1}{2} \qquad (4.29)$$

However the expression $\frac{S_{C_R}}{C_R}$ is more complicated. The precision index for C_R can be estimated from:

$$C_R = f\left(C_p\right) \qquad (4.30)$$

$$\left(\frac{S_{C_R}}{C_R}\right) = \frac{\delta C_R}{\delta C_P} \cdot \frac{C_P}{C_R} \cdot \frac{S_{C_P}}{C_P} = \frac{\delta C_R}{\delta C_P} \cdot \frac{S_{C_P}}{C_R} \qquad (4.31)$$

Where $\frac{\delta C_R}{\delta C_P}$ can either be estimated numerically, or by approximating C_R as C_{*i} and finding its derivative with respect to γ (C_P). Both of these approaches yielded the same result for S_{C_R}. A summary of the influence coefficients for equation 4.28 is given in table table 4.6. Table 4.6 shows the values for the influence coefficients, precision indices, bias limits and 95% uncertainty estimates.

Similarly the Bias limits can be defined as:

59

Table 4.4: Pretest Mass Flow Uncertainties

Quantity	C_*	B	S	v	U_{95}
T_1	0.5	0.1%	0.05%	30+	0.14%
P_1	1.0	0.15%	0.07%	30+	0.18%
C_d	1.0	0.35%	0.0%	30+	0.35%
C_p	0.1	0.2%	-	-	0.02%
$\dot{m}$	-	0.385%	0.074%	30+	0.41%

$$B_{\dot{m}} = \sqrt{\left(\frac{\delta \dot{m}}{\delta C_d} \cdot B_{C_d}\right)^2 + \left(\frac{\delta \dot{m}}{\delta C_R} \cdot B_{C_R}\right)^2 + \left(\frac{\delta \dot{m}}{\delta P_0} \cdot B_{P_0}\right)^2 + \left(\frac{\delta \dot{m}}{\delta T_0} \cdot B_{T_0}\right)^2} \qquad (4.32)$$

In terms of the influence coefficients:

$$\frac{B_{\dot{m}}}{\dot{m}} = \sqrt{\left(C_{C_d} \cdot \frac{B_{C_d}}{C_d}\right)^2 + \left(C_{C_R} \cdot \frac{B_{C_R}}{C_R}\right)^2 + \left(C_{P_0} \cdot \frac{B_{P_0}}{P_0}\right)^2 + \left(C_{T_0} \cdot \frac{B_{T_0}}{T_0}\right)^2} \qquad (4.33)$$

The uncertainty due to the transient correction will be small, as the maximum value of the correction is approximately 4% over the area of interest. The bias in estimating the compartment volumes is the main source of error. Fortunately, the largest volumes are the easiest to estimate. The bias for the correction will be approximately 1.0%. This is not significant source of uncertainty compared to the other discharge coefficient of the nozzle.

4.7 Summary

A critical flow venturi has been installed in MIT blowdown turbine facility in order to measure the turbine mass flow. An independent laboratory calibrated the discharge coefficient of the nozzle with stated uncertainty of ±0.35%. Two independent approaches were used to estimate the influence of real gas effects on the predicted nozzle mass flow rate, both of which produced the same result. An analytical model was used to determine the magnitude of the transient correction that relates the turbine mass flow to the nozzle flow rate. This

was shown to be a small correction. An uncertainty analysis of the mass flow measurement estimates the measurement uncertainty to be ±0.41%.
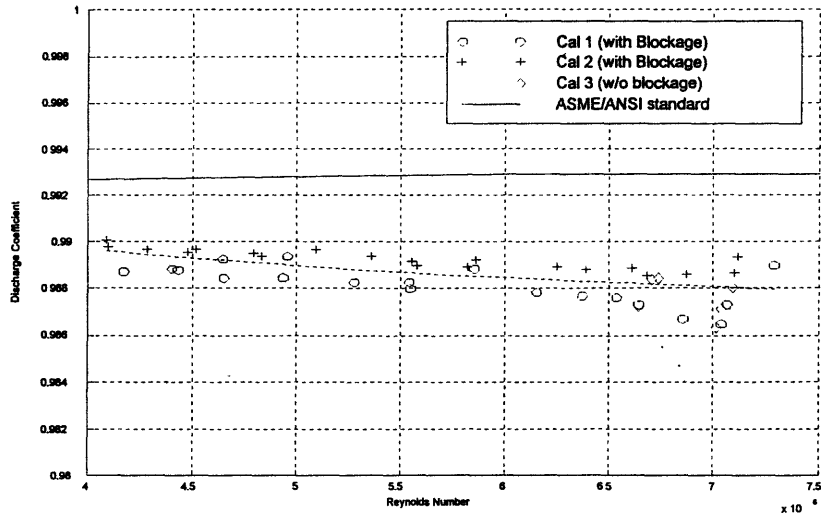
Figure 4-1: Critical Flow Venturi Calibration Results
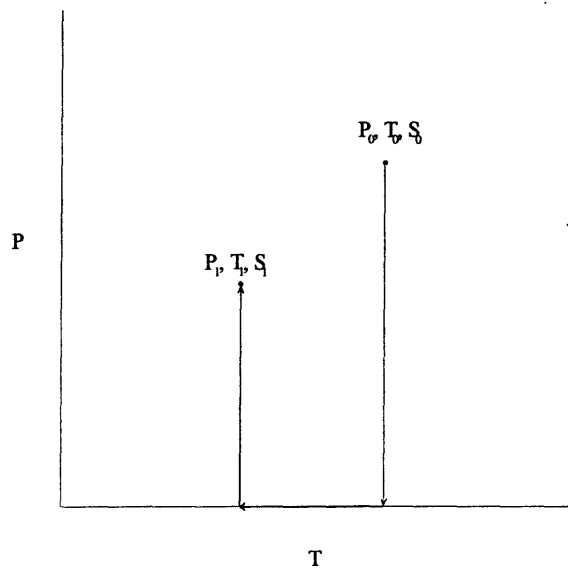
Figure 4-2: Integration path for Entropy and Enthalpy equations
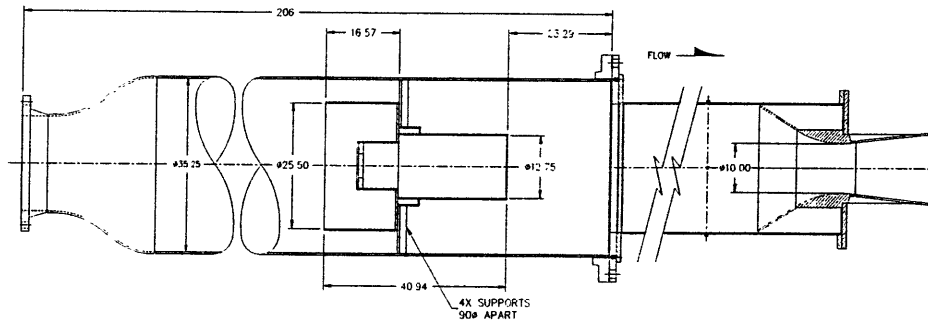
Figure 4-3: Venturi calibration with simulated blockage
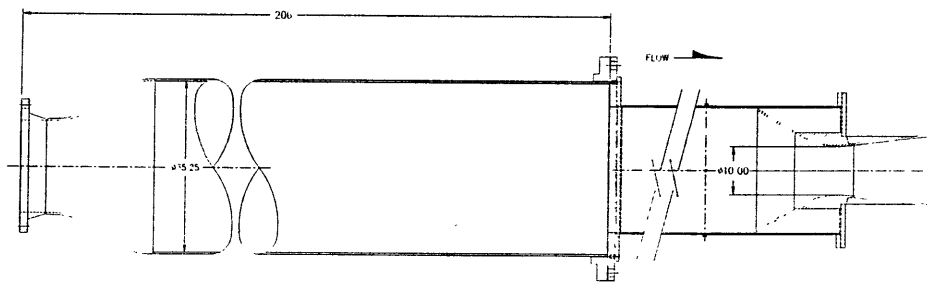
Figure 4-4: Venturi calibration without simulated blockage
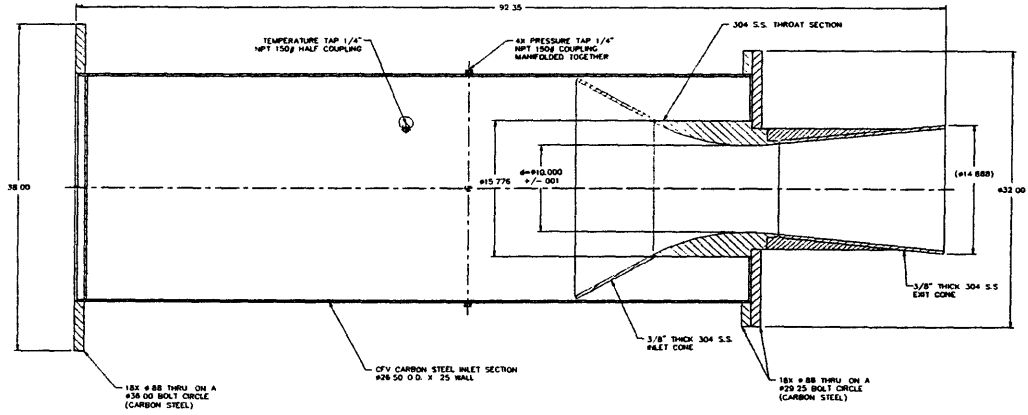
Figure 4-5: Critical Flow Venturi Assembly
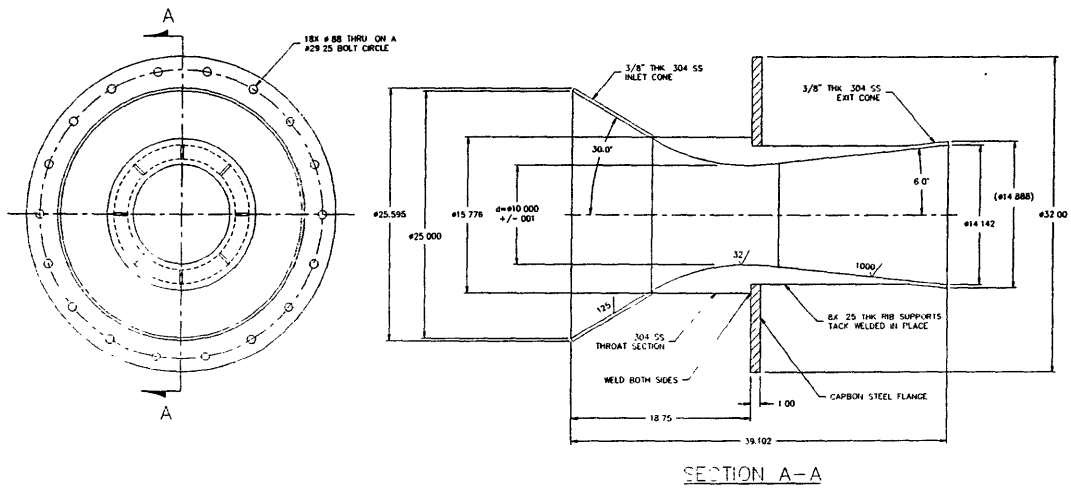
Figure 4-6: Nozzle Detail

A = Area
V = Volume
m = Mass Flow
P = Pressure
T = Temperature

Dump Tank

V_5, P_5, T_5
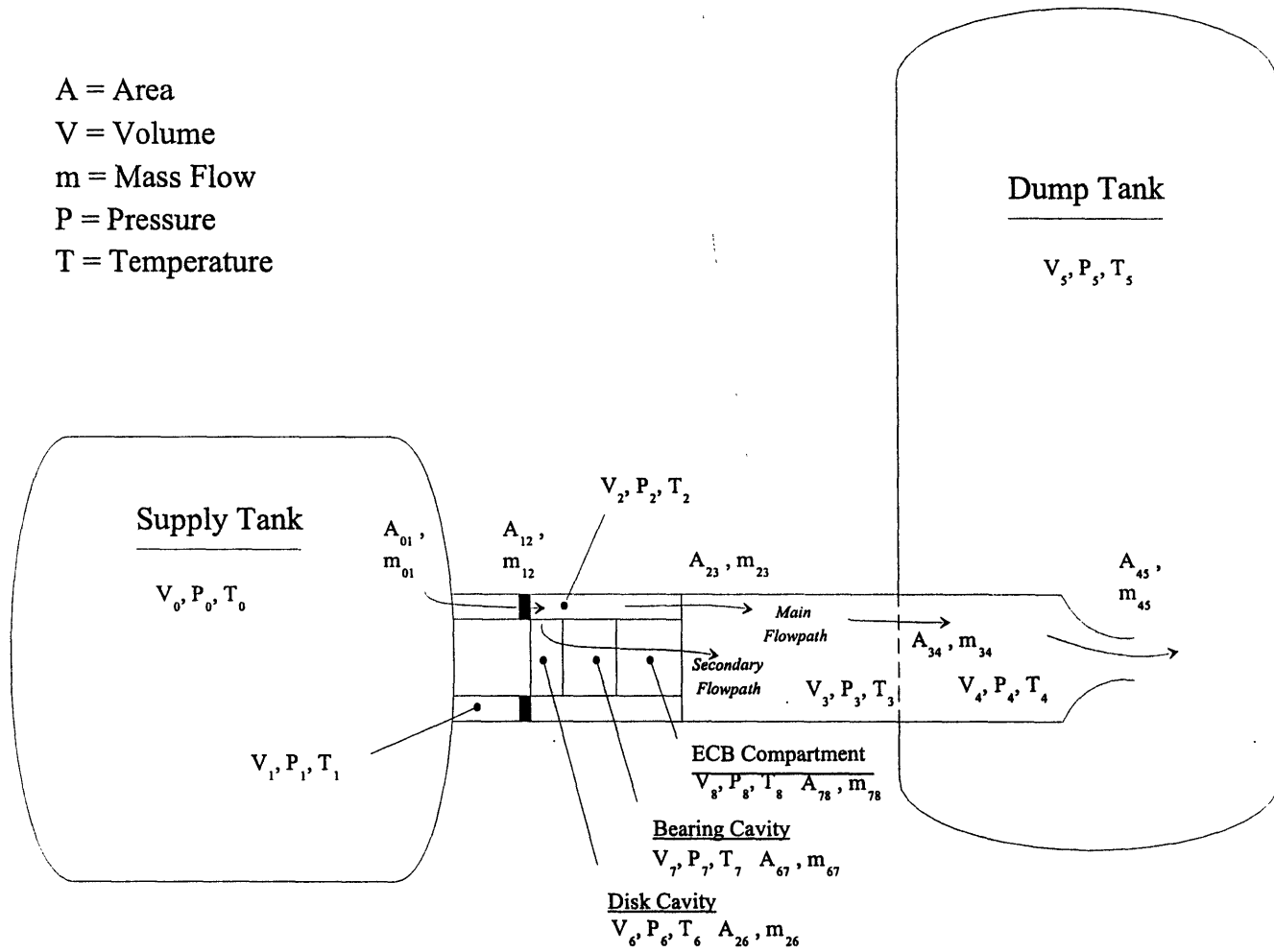
Figure 4-7: Blowdown Model Schematic

V_2, P_2, T_2

Supply Tank

V_0, P_0, T_0

A_{01}, m_{01}

A_{12}, m_{12}

A_{23}, m_{23}

A_{45}, m_{45}

Main Flowpath

Secondary Flowpath

A_{34}, m_{34}

V_3, P_3, T_3

V_4, P_4, T_4

V_1, P_1, T_1

ECB Compartment
$V_8, P_8, T_8 \quad A_{78}, m_{78}$

Bearing Cavity
$V_7, P_7, T_7 \quad A_{67}, m_{67}$

Disk Cavity
$V_6, P_6, T_6 \quad A_{26}, m_{26}$
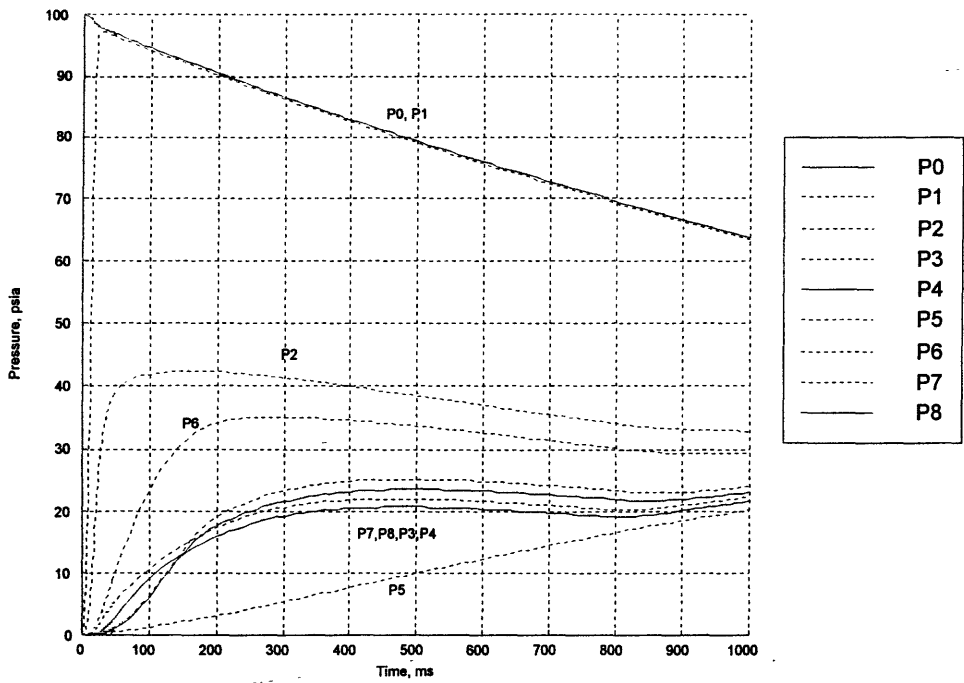
Figure 4-8: Compartment Pressures (Case 1)
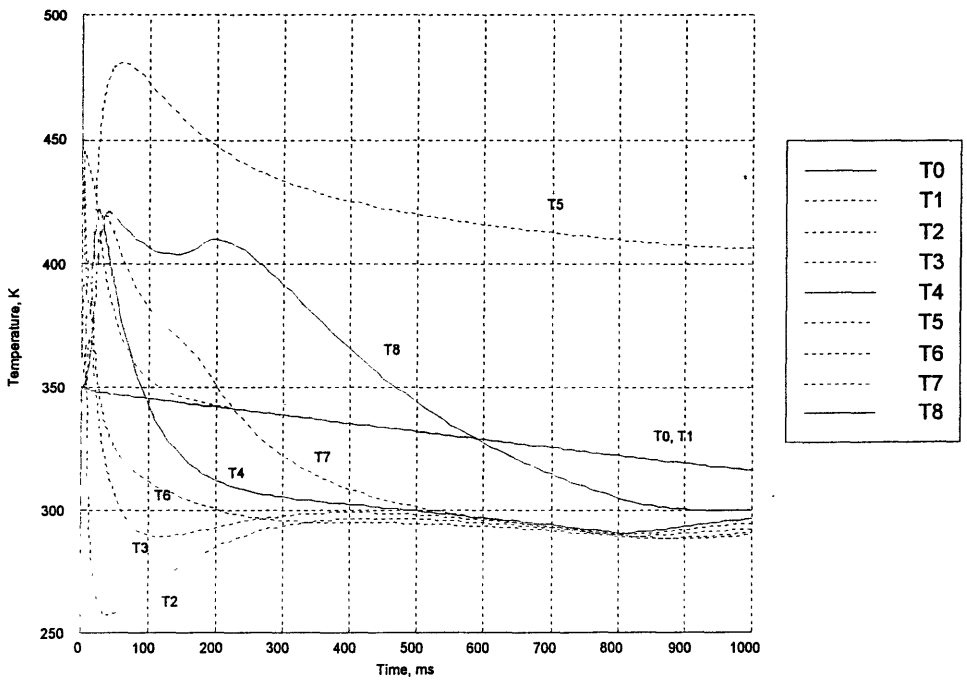
Figure 4-9: Compartment Temperatures (Case 1)
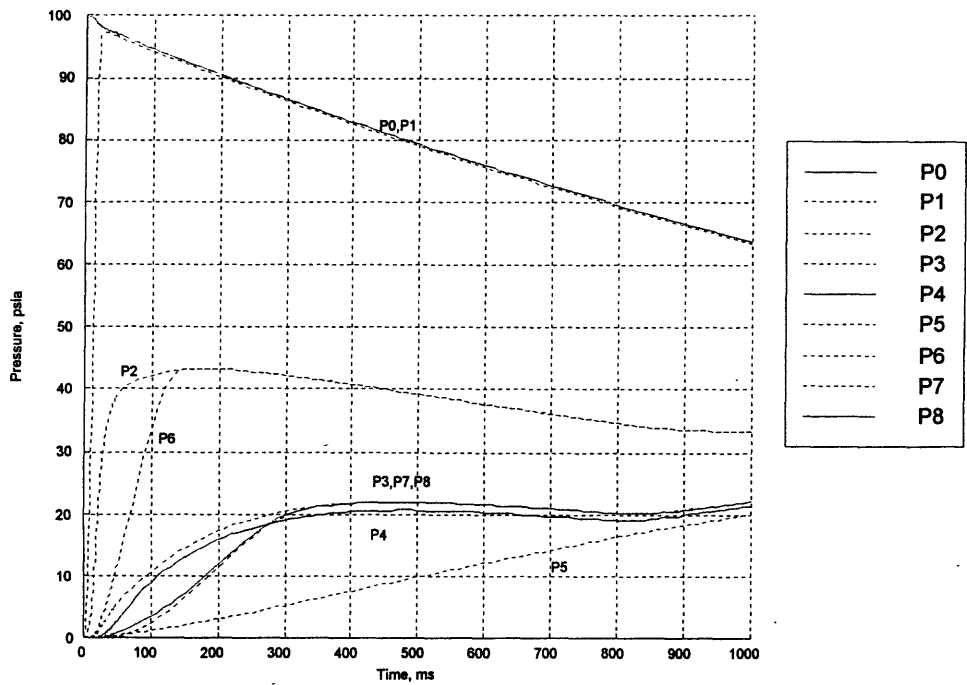
Figure 4-10: Compartment Pressures (Case 2)
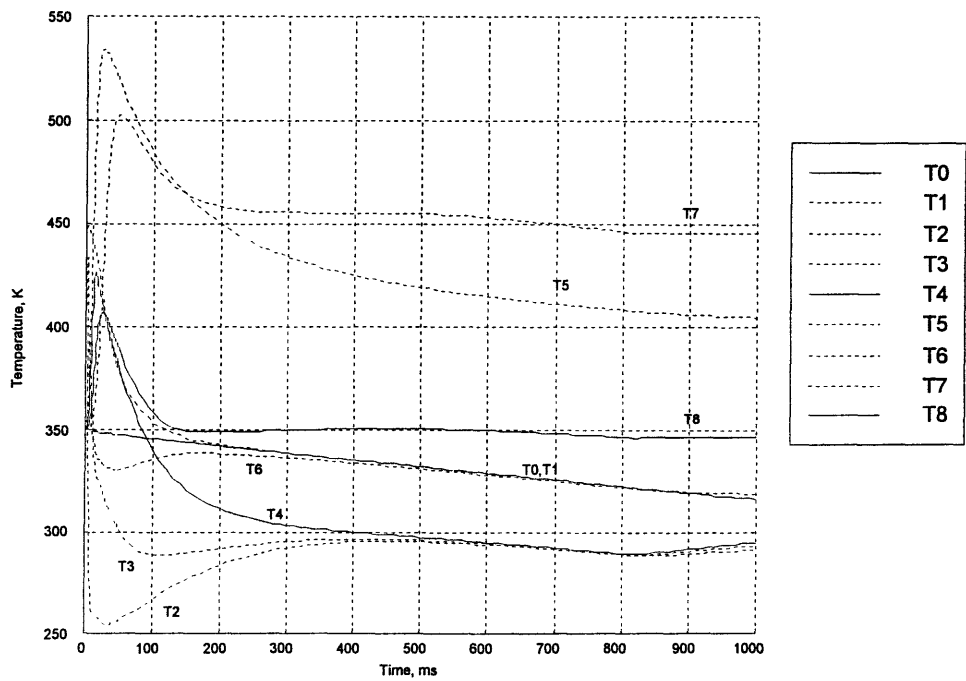
Figure 4-11: Compartment Temperatures (Case 2)

67
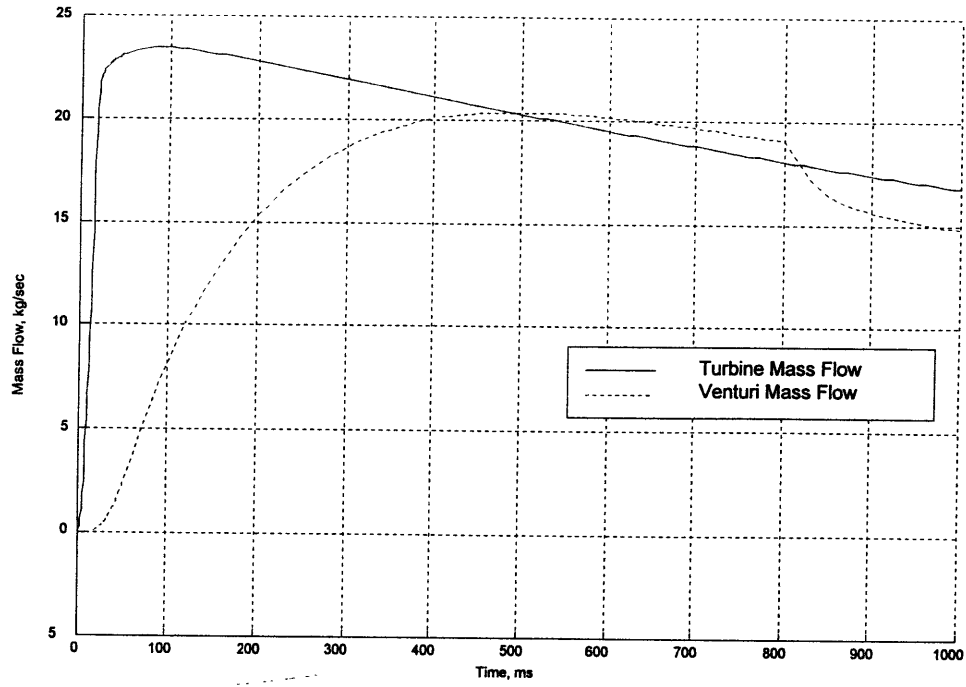
Figure 4-12: Turbine Mass Flow and Venturi Mass Flow
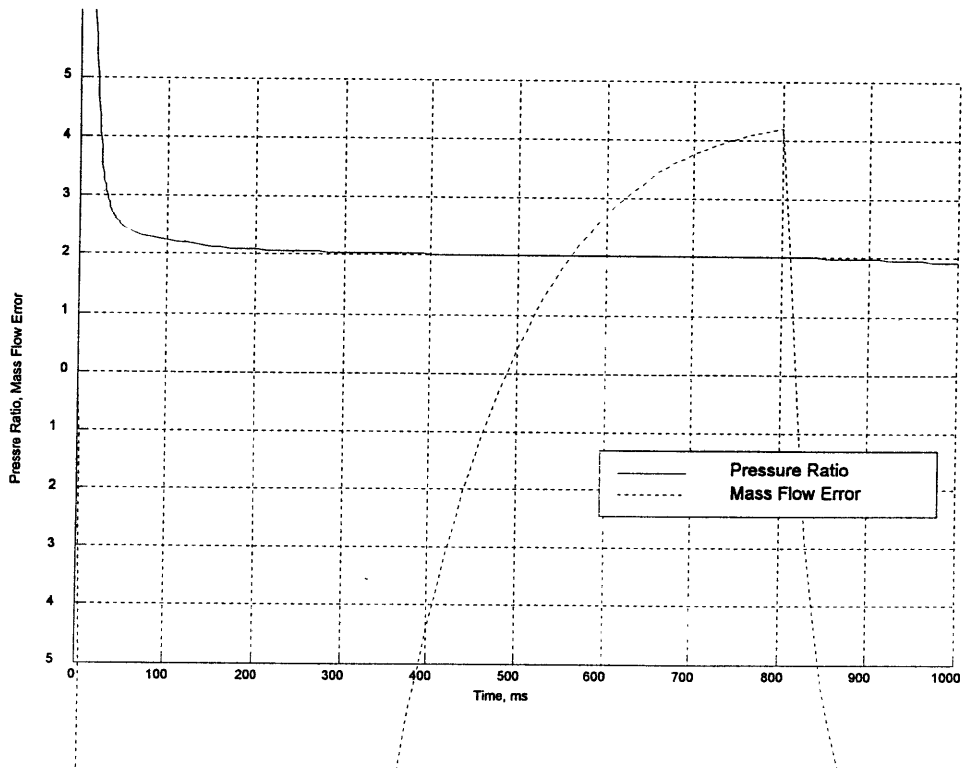
Figure 4-13: Pressure Ratio and $\dot{m}_{Stored}$ Total
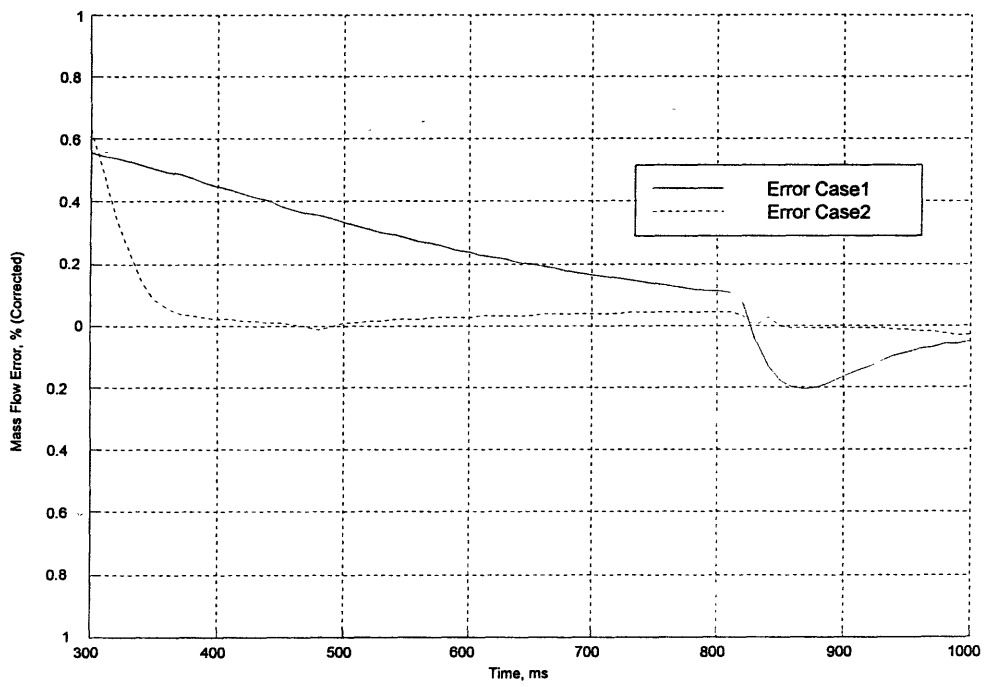
Figure 4-14: Mass Flow Error Case1 vs Case2

Chapter 5

Aerodynamic Performance Measurements

5.1 Introduction

This chapter describes the measurement of turbine aerodynamic performance in the Blow-down Turbine Facility. Firstly the adiabatic turbine efficiency is defined. The adiabatic efficiency cannot be measured directly in a short duration facility. A small non-adiabatic correction must be applied to the measured efficiency. This non-adiabatic correction is discussed in detail. The uncertainty analysis for the efficiency measurement and the test results are presented.

5.2 Adiabatic Efficiency

The turbine being tested is operating in a fully scaled environment. Neither the full-scale turbine nor the MIT turbines, operate under adiabatic conditions. However, adiabatic efficiency is generally used as a benchmark for turbine performance as it distinguishes the influence of heat transfer from the other losses. The turbine tested can be compared with data taken form conventional adiabatic testing facilities. More importantly, the data will

primarily be used to validate computational fluid dynamics codes, for which the adiabatic efficiency is more useful.

In this study the subscripts 1 and 2 represent the turbine inlet and outlet stagnation conditions respectively (only stagnation conditions will be referred to here). Thus, h_1 and h_2 are the inlet and outlet enthalpies, T_1 and T_2 the temperatures, and P_1 and P_2 the pressures. This follows the notation used in reference [4].

In this study, the real gas properties for the test gas are used. One disadvantage of testing in a low temperature facility such as this is that many of the test gases available exhibit significant non-ideal gas effects at low temperature (which are different than thoes in an engine). In the case of the turbine being studied, the difference between the change in enthalpy is approximately 0.5%, when comparing assuming real versus ideal gas properties for the test conditions. This, however, is significant enough that it needs to be considered for the efficiency measurement, yet at the same time it is also small enough that so that ideal gas simplifications can readily be used for the purposed of uncertainty analysis. This is very useful as it simplifies the algebra while maintaining physical insight into the problem.

Real turbines generate entropy so they produce less work than the ideal. For an adiabatic turbine with losses, the outlet enthalpy is h_{2ad} with a corresponding work output of W_{ad}, where $W_{ad} = h_1 - h_{2ad}$. The adiabatic efficiency of this turbine can be defined as:

$$\eta_{ad} = \frac{h_1 - h_{2ad}}{h_1 - h_{2is}} \tag{5.1}$$

For a perfect gas with constant properties with constant properties, this reduces to the familiar form:

$$\eta_{ad} = \frac{1 - \frac{T_{2ad}}{T_1}}{1 - \left(\frac{P_2}{P_1}\right)^{\frac{\gamma-1}{\gamma}}} \tag{5.2}$$

The shaft efficiency is defined as the ratio of the actual power to the ideal power extracted form the turbine:

71

$$\eta_s = \frac{T \cdot \omega}{\dot{m}(h\,(T_1, P_1) - h\,(T_2, P_2))} \tag{5.3}$$

The enthalpies are found from NIST 14 (see [15]), for the gas mixture at the test temperature and pressure. For the purposes uncertainty analysis, the ideal gas form of equation 5.3 was used:

$$\eta_s = \frac{T \cdot \omega}{\dot{m}\,C_p T_1 \left(1 - \left(\frac{P_2}{P_1}\right)^{\frac{\gamma-1}{\gamma}}\right)} = \frac{T \cdot \omega}{\dot{m}\,C_p T_1 \left(1 - \pi^{-\frac{R}{C_p}}\right)} \tag{5.4}$$

Where T, ω, $\dot{m}$, and C_p are the torque, speed, mass flow, and specific heat capacity, respectively.

In this paper, we are concerned with non-ideal turbines that are non-adiabatic. If the total heat loss to the walls is Q_w, then the work output in this case is:

$$W = h_1 - (h_2 + Q_w) \tag{5.5}$$

Where h_1 and h_2 are the enthalpies measured in the test. If the efficiency of this turbine was computed from the gas inlet and outlet enthalpies the indicated efficiency of the turbine, η_{ind}, is:

$$\eta_{ind} = \frac{h_1 - h_2}{h_1 - h_{2,is}} \tag{5.6}$$

The torque efficiency, defined as the measured work divided by the ideal change in enthalpy

$$\eta_s = \frac{W}{h_1 - h_{2,is}} = \frac{h_1 - h_2 - Q_w}{h_1 - h_{2,is}} = \eta_{ind} - \frac{Q_w}{h_1 - h_{2,is}} \tag{5.7}$$

The adiabatic performance is then related to the non-adiabatic test results as

$$\eta_{ad} = \frac{h_1 - h_2 + h_2 - h_{2,ad}}{h_1 - h_{2,is}} = \eta_{ind} - \frac{h_{2,ad} - h_2}{h_1 - h_{2,is}} \tag{5.8}$$

72

Or:

$$\eta_{ad} = \eta_s + \frac{Q_w}{h_1 - h_{2,is}} - \frac{h_{2,ad} - h_2}{h_1 - h_{2,is}} \qquad (5.9)$$

Thus, we must know both the heat transferred to the walls, Q_w, and how to form an estimate of the adiabatic exit enthalpy, h_{2ad}, in order to correct the short duration, non-adiabatic rig measurement to an equivalent adiabatic efficiency.

At this point, thermodynamics alone is not sufficient to estimate η_{ad}. We must invoke some turbine fluid mechanics. First, consider how to estimate the total heat load. This can be done by one of several manners: (1) comparison of the shaft power with the measured aerodynamic rake enthalpy; (2) a one- dimensional compressible flow analysis utilizing Reynolds analogy; (3) a two- dimensional flow analysis with heat transfer; (4) by direct experimental measurement of Q_w.

Next, we must estimate the adiabatic exit enthalpy, which is not so simple. There are two sources of entropy that must be quantified: that which is due to heat transfer and that due to the influence of the heat transfer upon the turbine fluid mechanics. To calculate the entropy produced directly by heat transfer, we must know the temperature at which heat is extracted. Except for the shaft and rake power extraction case, all of the above techniques should yield the heat transfer and temperature distributions with similar accuracy. The shaft and rake case will yield a more accurate heat load but little idea of the extraction temperature. By estimating the extraction temperature to either the inlet relative total temperature for the nozzle, or the exit static temperature of the rotor, its influence can be bounded. The entropy change (positive or negative) by the modification of the flow due to cooling, we believe to be of second order compared to the direct entropy change due to cooling.

5.3 Estimation of Adiabatic Exit Enthalpy, h_{2ad}

In a turbomachine we define the isentropic efficiency as the ratio of the actual work to the isentropic work. Thus the only factors that change this efficiency are departures form isentropic flow. These may either be heat transfer or thermodynamic irreversibility. The only rational measure of loss in a machine is entropy creation. Entropy is an unfamiliar quantity because it cannot be seen or measured directly, its values can only be inferred by the measurement of other properties. Basic thermodynamics tells us that for a single-phase fluid, entropy is a function of only two other thermodynamic properties such as temperature and pressure (Denton [17]). For a perfect gas the relationship between entropy and temperature and pressure is:

$$ S - S_{Ref} = C_p \, ln \left(\frac{T}{T_{Ref}} \right) - R \, ln \left(\frac{P}{P_{Ref}} \right) \tag{5.10} $$

Note, the pressures and temperatures in these equations may be either all static or all stagnation values because, by definition, the change from static to stagnation conditions is isentropic. Equation 5.10 can be rearranged to give:

$$ \frac{P_2}{P_1} = \left(e^{-\frac{\Delta S}{C_p}} \left(\frac{T_1}{T_2} \right) \right)^{\frac{\gamma}{\gamma - 1}} \tag{5.11} $$

The entropy generation due to heat transfer across a finite temperature gradient can be estimated from:

$$ \Delta S_Q = \int_1^2 \left(\frac{\delta Q}{T} \right)_{rev} = \frac{Q_w}{T^*} \tag{5.12} $$

Where T* is the temperature at which the heat is extracted. The adiabatic entropy change is defined as the total entropy change, less the entropy change due to heat transfer:

$$ \Delta S_{ad} = \Delta S_T - \Delta S_Q \tag{5.13} $$

The adiabatic exit temperature can be estimated using equation 5.11 to equate the

74

adiabatic and non-adiabatic cases for the same pressure ratio:

$$e^{\frac{\Delta S_{ad}}{C_p}} \left(\frac{T_1}{T_{ad}}\right) = e^{-\frac{\Delta S_T}{C_p} - \frac{\Delta S_Q}{C_p}} \left(\frac{T_1}{T_{ad}}\right) = e^{-\frac{\Delta S_T}{C_p}} \left(\frac{T_1}{T_2}\right) \qquad (5.14)$$

If $e^{-\frac{\Delta S_T}{C_p}}$ is replaced by its MacLaurin series expansion, with the higher order terms dropped, equation 5.14 reduces to:

$$T_{2ad} = T_2 \left(1 + \frac{Q_w}{T^* C_p}\right) \qquad (5.15)$$

or:

$$h_{2ad} = h_2 + Q_w \left(\frac{T_2}{T^*}\right) \qquad (5.16)$$

This can then be substituted into equation 5.9 to yield:

$$\eta_{ad} = \eta_s + \frac{Q_w}{h_1 - h_{2,is}} - \frac{h_2 + Q_w \left(\frac{T_2}{T^*}\right) - h_2}{h_1 - h_{2,is}} \qquad (5.17)$$

$$\eta_{ad} = \eta_s + \frac{Q_w}{h_1 - h_{2,is}} \left(1 - \frac{T_2}{T^*}\right) \qquad (5.18)$$

Equation 5.18 is very useful as it shows the effect of heat transfer on the adiabatic correction. Equation 5.19 can be derived by taking the T^* as the mean of the turbine inlet and outlet temperatures, and substituting 5.5 into 5.18:

$$\Delta\eta_{ad} = \eta_{ad} - \eta_s = (\eta_s - \eta_{ind}) \left(\frac{1 - \tau}{1 + \tau}\right) \qquad (5.19)$$

Equation 5.19 is very useful for the purposes of uncertainty analysis, as data for the uncertainty of η_s and η_{ind} are already available. The uncertainty values for η_{ind} are reported by Cai [8], and the values for η_s can be found in section 5.4. If the uncertainty of $\left(\frac{1-\tau}{1+\tau}\right)$ is taken to be $\pm 100\%$, this bounds T^* between T_2 and T_1. The results of the uncertainty analysis for $\Delta\eta_{ad}$ is contained in table 5.3. The heat load is estimated to be 2% of the ideal

Table 5.1: Adiabatic Correction Uncertainty

Parameter	Value	Bias, B	Precision, S	Uncertainty, U_{95}
$\frac{Q}{h_1 - h_{2is}}$	0.02	-	-	-
τ	0.87	-	-	-
π	2	-	-	-
T_1	$350^\circ K$	-	-	-
η_s	0.90	0.0040	0.0020	0.62%
η_{ind}	0.92	0.0041	0.0015	0.55%
$\left(\frac{1-\tau}{1+\tau}\right)$	0.070	0.070	-	100%
$\Delta\eta_{ad}$	0.0014	0.0015	0.0002	107%
η_{ad}	0.8986	0.0043	0.0020	0.65%

enthalpy drop across the turbine (for $T_1 = 350^\circ K$). The results show that the uncertainty in $\Delta\eta_{ad}$ is approximately equal to its magnitude. The actual uncertainty is small compared to the uncertainty in η_s and will not significantly affect accuracy of the efficiency mesurement unless Q is larger. Also, assuming an uncertainty of 100% for $\left(\frac{1-\tau}{1+\tau}\right)$ is very conservative. For back-to-back tests $\Delta\eta_{ad}$ can be neglected.

5.4 Uncertainty Analysis

General

All measurements have errors. These errors are the differences between the measurement and the true value. The uncertainty is an estimate of the test error, which in most cases would not be exceeded. Measurement error, δ, had two components: a fixed error β', and a random error ϵ.

Precision (Random Error): Random error is seen in repeated meaasurements of the same thing. Measurements do not and are not and are not expected to agree exactly. There are numerous small effects that cause disagreements. The precision of a measurement process is determined by the variation between repeated measurements. The standard deviation σ is used to determine the precision error ϵ. A large standard deviation means large scatter

in the measurements. The statistic S is calculated to estimate the standard σ and is called the precision index.

Bias (Fixed Error): The second component of error, bias β', is the error that remains constant for the duration of the test. In repeated measurements, each measurement would have the same bias. The bias cannot be determined unless the measurements are compared to the true value of the quantity measured.

Measurement Uncertainty Interval: For simplicity, a single number is (some combination of bias and precision) is needed to express a reasonable limit for the total error. The single number must have a simple interpretation (like the largest error reasonably expected) and be useful without complex explanation. It is impossible to define a single rigorous statistic because the bias is an upper limit based on judgment which has unknown characteristics. Any function of these two numbers must be a hybrid combination of an unknown quantity (bias) and a statistic (precision). If both numbers were statistics, a confidence interval would be recommended. Confidence levels of 95% and 99% would be available at the discretion of the analyst. Although rigorous statistical confidence levels are not available, two uncertainty intervals are recommended by ASME/ANSI, analogous to 95% and 99% levels.

Where t_{95} is the 95th percentile point on the two tailed Student's t distribution. The t value is a function of the number of degrees of freedom (sample size) v used in calculating S. For small samples t is large and for large samples t is smaller, approaching 1.96 in the lower limit. The use of t inflates the limit U to reduce risk of understating σ when a small sample is used to calculate S. Since 30 degrees of freedom v yields a t of 2.04 and infinite degrees of freedom yields a t of 1.96, an arbitrary selection of t=2.0 for values of v from 30 to infinity is made, i.e.

$$U_{95} = \sqrt{B^2 + (t_{95}S)^2} \tag{5.20}$$

Pre-test versus Post-test Uncertainty Analysis

The accuracy of the test is often part of the test requirement. Such requirements are defined by pre-test uncertainty analysis. This allows corrective action to be taken before the test to improve the uncertainties when they are too large. It is based on data and information that exists before the test, such as calibration histories, previous tests with similar instrumentation, prior measurement uncertainty analysis, and expert opinion. With complex tests, there are often alternatives to evaluate, including different test design configurations, instrumentation layouts, alternative calibration procedures, etc. Pre-test analysis will identify the most accurate test method. A post-test measurement uncertainty analysis is required to confirm the pre-test estimates or to identify problems. Comparison of test results with the pre-test analysis is an excellent data validity check. The precision of repeated points or redundant instrumentation should not be significantly larger than pre-test estimates. The final uncertainty interval should be based on post-test analysis.

Back-To-Back Testing

The objective of back to back testing is to determine the net effect of a design change most accurately, i.e., with the smallest measurement uncertainty. The first test is run with a standard or baseline configuration. The second test is identical to the first except that the design change is substituted in the baseline configuration. The difference between the results of the two tests is an indication of the effect of the design change.

As long as we consider only the difference or net effect between the two tests, all the fixed, constant bias errors will cancel out. The measurement error is composed of precision errors only.

The efficiency uncertainty can be expressed as the following.

A Taylor series expansion of equation 5.3 yields equation 4.26 and 4.32 from which the measurement precision index and bias limits are calculated.

78

$$S_\eta = \sqrt{\left(\frac{\delta\eta}{\delta T} \cdot S_T\right)^2 + \left(\frac{\delta\eta}{\delta m} \cdot S_m\right)^2 + \left(\frac{\delta\eta}{\delta C_p} \cdot S_{C_p}\right)^2 + \left(\frac{\delta\eta}{\delta T_1} \cdot S_{T_1}\right)^2 + \left(\frac{\delta\eta}{\delta\pi} \cdot S_\pi\right)^2} \quad (5.21)$$

If we define the influence coefficient for each variable in equation 4.26 as:

$$C_* = \frac{\delta\eta}{\delta*} \cdot \frac{*}{\eta} \quad (5.22)$$

Then equation 4.26 can be rewritten as:

$$\frac{S_\eta}{\eta} = \sqrt{\left(C_T \cdot \frac{S_T}{T}\right)^2 + \left(C_m \cdot \frac{S_m}{m}\right)^2 + \left(C_{C_p} \cdot \frac{S_{C_p}}{C_p}\right)^2 + \left(C_T \cdot \frac{S_{T_1}}{T_1}\right)^2 + \left(C_\pi \cdot \frac{S_\pi}{\pi}\right)^2}$$
$$(5.23)$$

This is a more useful form than that of equation 4.26. The influence coefficient is a non-dimensional parameter that represents the how a given error source will be propagate to overall measurement error. The influence coefficient represents the relative amplification of that source error through equation 5.3. The sign of the influence coefficient is not important as the term is squared. The influence coefficients C_T, C_m and C_{T_1} are straightforward:

$$C_T = 1, C_m = -1, C_{T_1} = -1 \quad (5.24)$$

However the expressions C_{C_p} and C_π are considerably more complicated:

$$C_{C_p} = \left(1 + \frac{\pi^{\frac{R}{C_p}} \cdot R \cdot ln\left(\pi\right)}{c_p \cdot \left(1 - \pi^{\frac{R}{C_p}}\right)}\right) = \left(1 + \frac{\pi^{\frac{\gamma-1}{\gamma}} \cdot \frac{\gamma-1}{\gamma} \cdot ln\left(\pi\right)}{\left(1 - \pi^{\frac{\gamma-1}{\gamma}}\right)}\right) \quad (5.25)$$

Equations were derived using a symbolic differentiation program and the results were verified numerically using sample values for γ and π.

Table 5.2: Pretest Uncertainties

Quantity	C_*	$B_*/*$	$S_*/*$	v	U_{95}
T_1	1.0	0.01%	0.03%	30+	.06%
$\dot{m}$	1.0	0.33%	0.13%	30+	.41%
$\mathcal{T}$	1.0	0.10%	0.13%	30+	.28%
π	1.34	0.10%	0.15%	30+	.30%
C_p	0.07	0.20%	-	30+	.20%
η	-	0.37%	0.27%	30+	.65%

$$C_\pi = \frac{\pi^{\frac{R}{C_p}} \cdot R}{C_p \cdot \left(1 - \pi^{\frac{R}{C_p}}\right)} = \frac{\pi^{\frac{\gamma-1}{\gamma}} \cdot \frac{\gamma-1}{\gamma}}{\left(1 - \pi^{\frac{\gamma-1}{\gamma}}\right)} \qquad (5.26)$$

Similarly the Bias limits can be defined as:

$$B_\eta = \sqrt{\left(\frac{\delta\eta}{\delta\mathcal{T}} \cdot B_{\mathcal{T}}\right)^2 + \left(\frac{\delta\eta}{\delta m} \cdot B_m\right)^2 + \left(\frac{\delta\eta}{\delta C_p} \cdot B_{C_p}\right)^2 + \left(\frac{\delta\eta}{\delta T_1} \cdot B_{T_1}\right)^2 + \left(\frac{\delta\eta}{\delta\pi} \cdot B_\pi\right)^2}$$
$$(5.27)$$

In terms of the influence coefficients:

$$\frac{B_\eta}{\eta} = \sqrt{\left(C_{\mathcal{T}} \cdot \frac{B_{\mathcal{T}}}{\mathcal{T}}\right)^2 + \left(C_m \cdot \frac{B_m}{m}\right)^2 + \left(C_{C_p} \cdot \frac{B_{C_p}}{C_p}\right)^2 + \left(C_{\mathcal{T}} \cdot \frac{B_{T_1}}{T_1}\right)^2 + \left(C_\pi \cdot \frac{B_\pi}{\pi}\right)^2}$$
$$(5.28)$$

Table 5.4 shows sample values for the influence coefficients. This shows that the uncertainty in pressure ratio will be amplified whereas the uncertainty in C_p will be significantly reduced.

Table 5.4 contains a summary of the pretest uncertainties for $\mathcal{T}$, m, T_{T_1}, C_p, and π. The estimated uncertainty for η will be 1.0% at a 95% confidence interval. For back-to-back test the uncertainty for changes in η will be 0.5%.

The values for uncertainty in $\mathcal{T}$ and π are obtained by pre test calibrations by Cai [8].

The uncertainties for T and $\dot{m}$ are discussed in chapters 3 and 4.

The following guideline to estimate the uncertainty in C_p was proposed by Friend [16]. The bias limit for the C_p of CO_2 under ideal gas conditions is +/-0.1%, however the bias limit is significantly higher if real gas effects are important. NIST proposed that the bias limit be increased based on the deviation of CO_2 from ideal gas behavior. A limit of 5% uncertainty for the difference from ideal gas properties was proposed as a conservative estimate of the bias limit. In our case the difference from ideal gas behavior is approx. 2%, so the bias limit for the C_p of CO_2 is +/- 0.2%. In tests where the test gas is a mixture, the uncertainty of the composition must also be examined.
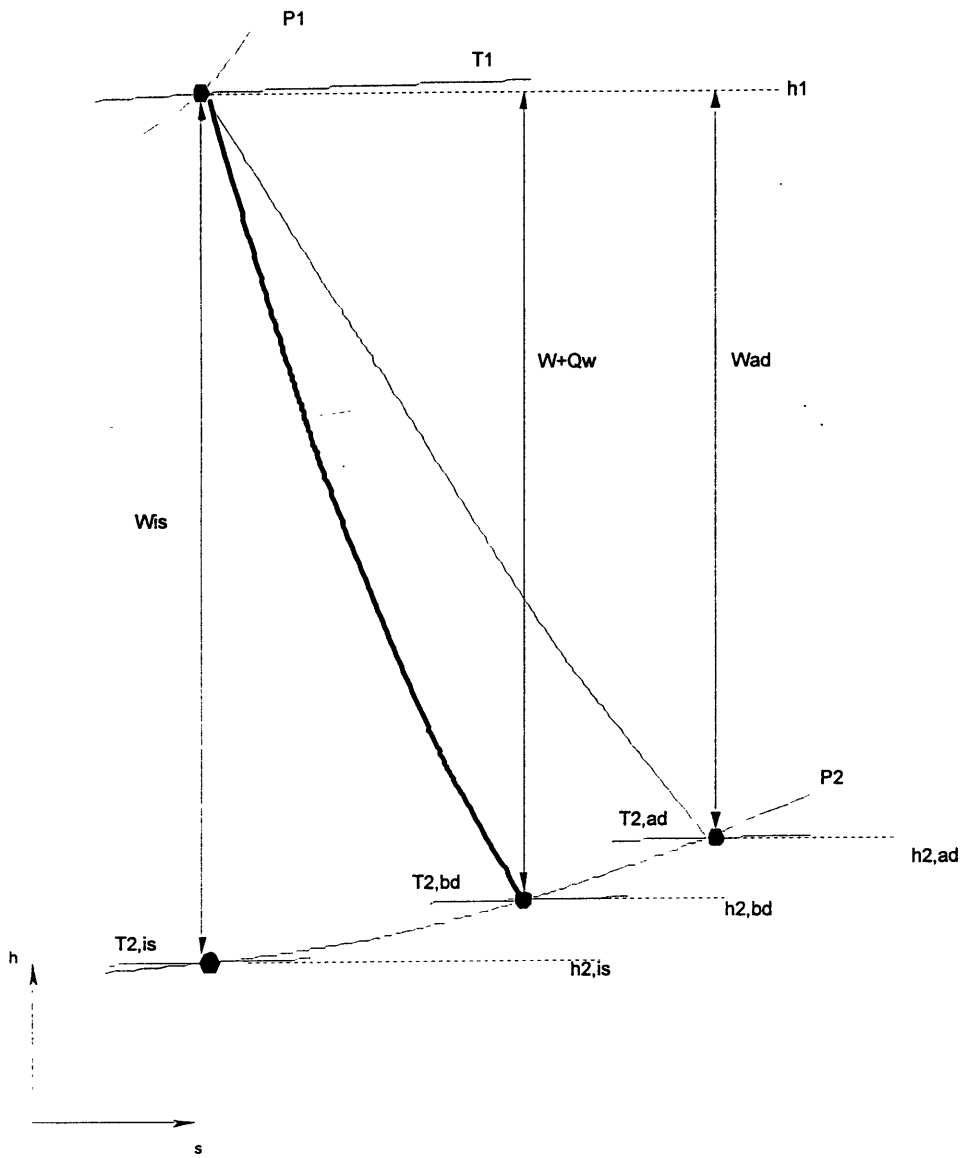
Figure 5-1: Turbine H-S Diagram

Chapter 6

Conclusion

6.1 Summary

Extensive modifications have been made to the MIT Blowdown Turbine Facility in order to make aerodynamic performance measurements. The turbine stage has been designed and fabricated along with the turbine disks, the rotating seal, and instrumentation ring. The new turbine stage has been tested under design conditions and operates flawlessly.

The Eddy Current Brake, which absorbs the power generated by the turbine, was modified so that the torque transmitted from the rotor could be measured. The torque meter was calibrated statically. Static calibrations were repeated several months apart and the results proved to be very consistent. The inertia of the rotating parts was estimated by braking the rotor in vacuum using the Eddy Current Brake. The inertia was measured at several different brake settings. As the inertia of the system is constant, his is a way to test the repeatability of the torque meter. This test also verified that the brake current level did not affect the torque meter results. The estimated uncertainty for the torque meter is 0.27%.

A critical flow venturi has been designed and fabricated to measure the mass flow through the turbine. The discharge coefficient of the venturi was calibrated by an independent laboratory with an estimated uncertainty of 0.35%. An uncertainty analysis of the critical

flow venturi estimates the mass flow rate uncertainty to be 0.41% with a 95% confidence level. A method for determining the real gas effects in the nozzle has been outlined and implemented. The transient correction that relates the nozzle mass flow rate to the turbine mass flow rate is approximately 4%. The critical flow venturi has yet to be tested.

The difference between short duration testing and steady adiabatic test rigs has been analyzed and has been shown to be a small correction under typical test conditions. The uncertainty for η_s is estimated to be 0.65% with a 95% confidence level. The uncertainty for back-to-back tests that measure changes in efficiency is estimated to be 0.38%.

Appendix A

Critical Flow Venturi Calibration Report

This appendix contains the calibration report for the critical flow venturi. Three separate calibration runs were performed. The first two calibrations tested the nozzle with a simulated blockage in place. Two tests were preformed in order verify the calibration. The calibration repeated within approximately 0.1%. A third more limited test was performed in order to determine the importance of simulated blockage. Six test points were taken at the design point of the nozzle without the simulated blockage. There was no noticible difference between the two test configurations.

The discharge coefficients in the calibration report were calculated based on the static rathar than the total pressure upstrean of the nozzle. This simplification is acceptible if β is 0.25 or less, however for this nozzle β is 0.385. The discharge coeffecients presented in figure 4-1 and table 4.1 are calculated using the total upstream conditions.

The ratio of total to static pressure can be estimated by calculating the Mach number in the upstream duct, where the mass flow is estimated using the static pressure. The resulting expression A.1is a function of β and γ only. Under test conditions equation A.1 estimates P_t to 0.004%. The correction for defferent test conditions is proveded in table A.1.

Table A.1: Nozzle Total Pressure Correction

Test Condition	γ	$\frac{P_t}{P_s}$
Calibration	1.404	1.0052
Blowdown Test	1.279	1.0048
$\beta = 0.385$		

$$\frac{P_t}{P_s} = \left[1 + \beta^4 \left(\frac{\gamma - 1}{2} \right) \left(\frac{2}{\gamma + 1} \right)^{\left(\frac{\gamma+1}{\gamma-1} \right)} \right]^{\frac{\gamma}{\gamma-1}} \qquad (A.1)$$

CEESI

LABORATORY/OFFICE:
54043 County Rd. 37
Nunn, Colo. 80648
Phone: 970-897-2711
FAX: 970-897-2710

COLORADO ENGINEERING EXPERIMENT STATION, INC.

CERTIFICATE OF CALIBRATION

This calibration is traceable to the

NATIONAL INSTITUTE OF STANDARDS AND TECHNOLOGY

Model: CFV-416-SPCL-10.000-2d-SPCLIF-CS/304 Serial Number: 9961

For: Flow Systems, Inc. Order: 8648

Data File: 97FSY351 Disc: 1197-027 Date: 15 November 1997

The uncertainty in indicated flowrate is estimated to be +/- 0.35 % of reading to 95% confidence.

The calibration identified by the above CEESI data file was performed using standards
that are traceable to the National Institute of Standards and Technology.

This calibration was performed in accordance with the current revision of
PROC-10 and MIL-STD 45662A.

This Calibration is: [X] As Found   [X] As Left

Calibration performed by: _____

Quality Assurance

On behalf of Colorado Engineering
Experiment Station Inc.

Re-calibration is recommended to be no more than 12 months from the date of this Certificate.
This Certificate and accompanying data shall not be reproduced, except in full, without the written
consent of Colorado Engineering Experiment Station Inc.

COLORADO ENGINEERING
EXPERIMENT STATION, INC.

```
Calibration of a Critical Flow Venturi
Model: CFV-416-SPCL-10.000-2d-SPCLIF-CS/304    Serial Number:  9961
For:  Flow Systems, Inc.   Order:  8648
Data File:  97FSY351   Disc:  1197-027   Date:  15 November 1997
Inlet diameter: 26 inches   Throat diameter: 10 inches
Test gas: AIR   Standard density= .074915  lbm/cu-ft
   at standard conditions of 529.69 deg R, and 14.696 psia
Press: Inlet static pressure in psia
Temp: Inlet temperature in degrees Rankine
Cd: Coefficient of Discharge
Rey No: Throat Reynolds number
Flow: Mass flow in pounds per second
C*: Critical Flow Factor, dimensionless
Upstream Blockage was not present
```

L	Press	Temp	Cd	Rey No	Flow	C*
1	25.848	446.1	0.99406	7.2861E+006	5.0886E+001	0.6858
2	24.960	444.1	0.99237	7.0650E+006	4.9162E+001	0.6858
3	24.769	442.6	0.99157	7.0364E+006	4.8830E+001	0.6858
4	24.001	440.8	0.99177	6.8559E+006	4.7421E+001	0.6858
5	23.099	438.7	0.99238	6.6437E+006	4.5775E+001	0.6857
6	22.636	437.2	0.99271	6.5419E+006	4.4948E+001	0.6857
7	21.951	435.7	0.99277	6.3729E+006	4.3665E+001	0.6857
8	21.098	434.3	0.99292	6.1520E+006	4.2041E+001	0.6857
9	19.985	433.2	0.99394	5.8524E+006	3.9911E+001	0.6856
10	18.863	431.6	0.99310	5.5459E+006	3.7707E+001	0.6856
11	18.815	431.2	0.99337	5.5401E+006	3.7639E+001	0.6856
12	17.835	429.9	0.99336	5.2720E+006	3.5730E+001	0.6856
13	16.644	429.0	0.99355	4.9342E+006	3.3383E+001	0.6855
14	16.682	428.7	0.99448	4.9548E+006	3.3504E+001	0.6855
15	15.605	427.3	0.99353	4.6502E+006	3.1360E+001	0.6855
16	15.567	427.0	0.99436	4.6469E+006	3.1320E+001	0.6855
17	14.830	426.3	0.99388	4.4342E+006	2.9846E+001	0.6855
18	14.705	425.9	0.99394	4.4026E+006	2.9611E+001	0.6855
19	13.914	425.3	0.99380	4.1728E+006	2.8032E+001	0.6854

```
Average values for above results:
Temp: 433.41 Deg R       Viscosity: .00000086862 lbm/inch-sec
```

CEESI

LABORATORY/OFFICE:
54043 County Rd. 37
Nunn, Colo. 80648
Phone: 970-897-2711
FAX: 970-897-2710

COLORADO ENGINEERING EXPERIMENT STATION, INC.

CERTIFICATE OF CALIBRATION

This calibration is traceable to the

NATIONAL INSTITUTE OF STANDARDS AND TECHNOLOGY

Model: CFV-416-SPCL-10.000-2d-SPCLIF-CS/304   Serial Number: 9961

For: Flow Systems, Inc.   Order: 8648

Data File: 97FSY352   Disc: 1197-027   Date: 15 November 1997

The uncertainty in indicated flowrate is estimated to be +/- *0.35* % of reading to 95% confidence.

The calibration identified by the above CEESI data file was performed using standards
that are traceable to the National Institute of Standards and Technology.

This calibration was performed in accordance with the current revision of
PROC-10 and MIL-STD 45662A.

This Calibration is: [X] As Found   [X] As Left

Calibration performed by: _____

_____
Quality Assurance

_____
On behalf of Colorado Engineering
Experiment Station Inc.

Re-calibration is recommended to be no more than *12* months from the date of this Certificate.
This Certificate and accompanying data shall not be reproduced, except in full, without the written
consent of Colorado Engineering Experiment Station Inc.

COLORADO ENGINEERING
EXPERIMENT STATION, INC.

Calibration of a Critical Flow Venturi
Model: CFV-416-SPCL-10.000-2d-SPCLIF-CS/304   Serial Number: 9961
For: Flow Systems, Inc.   Order: 8648
Data File: 97FSY352   Disc: 1197-027   Date: 15 November 1997
Inlet diameter: 26 inches   Throat diameter: 10 inches
Test gas: AIR   Standard density= .074915 lbm/cu-ft
  at standard conditions of 529.69 deg R, and 14.696 psia
Press: Inlet static pressure in psia
Temp: Inlet temperature in degrees Rankine
Cd: Coefficient of Discharge
Rey No: Throat Reynolds number
Flow: Mass flow in pounds per second
C*: Critical Flow Factor, dimensionless
Upstream Blockage was not present

L	Press	Temp	Cd	Rey No	Flow	C*
1	26.067	457.4	0.99445	7.1140E+006	5.0695E+001	0.6857
2	25.818	454.6	0.99372	7.0974E+006	5.0328E+001	0.6857
3	24.834	452.3	0.99367	6.8717E+006	4.8529E+001	0.6857
4	24.043	450.8	0.99364	6.6815E+006	4.7060E+001	0.6857
5	23.729	449.8	0.99396	6.6155E+006	4.6512E+001	0.6857
6	22.832	448.4	0.99393	6.3909E+006	4.4819E+001	0.6857
7	22.262	447.2	0.99401	6.2536E+006	4.3762E+001	0.6857
8	19.789	445.9	0.99409	5.5800E+006	3.8956E+001	0.6856
9	19.691	445.6	0.99424	5.5579E+006	3.8781E+001	0.6856
10	20.700	444.6	0.99430	5.8607E+006	4.0819E+001	0.6856
11	20.482	443.4	0.99402	5.8179E+006	4.0433E+001	0.6856
12	18.795	442.1	0.99449	5.3612E+006	3.7171E+001	0.6856
13	17.801	441.2	0.99476	5.0925E+006	3.5250E+001	0.6855
14	16.867	440.4	0.99448	4.8353E+006	3.3420E+001	0.6855
15	16.693	440.0	0.99461	4.7917E+006	3.3094E+001	0.6855
16	15.698	439.2	0.99478	4.5173E+006	3.1153E+001	0.6855
17	15.550	438.9	0.99467	4.4784E+006	3.0867E+001	0.6855
18	14.853	438.5	0.99477	4.2829E+006	2.9498E+001	0.6854
19	14.182	438.0	0.99492	4.0961E+006	2.8185E+001	0.6854
20	14.130	437.7	0.99517	4.0857E+006	2.8098E+001	0.6854

Average values for above results:
Temp: 444.79 Deg R   Viscosity: .0000008871 lbm/inch-sec

COLORADO ENGINEERING
EXPERIMENT STATION, INC.

CERTIFICATE OF CALIBRATION

This calibration is traceable to the

NATIONAL INSTITUTE OF STANDARDS AND TECHNOLOGY

Model: CFV-416-SPCL-10.000-2d-SPCLIF-CS/304   Serial Number: 9961

For: Flow Systems, Inc.   Order: 8648

Data File: 97FSY353   Disc: 1197-027   Date: 17 November 1997

The uncertainty in indicated flowrate is estimated to be +/- $.35$ % of reading to 95% confidence.

The calibration identified by the above CEESI data file was performed using standards
that are traceable to the National Institute of Standards and Technology.

This calibration was performed in accordance with the current revision of
PROC-10 and MIL-STD 45662A.

This Calibration is: [X] As Found   [X] As Left

Calibration performed by: _____

Quality Assurance _____

On behalf of Colorado Engineering
Experiment Station Inc.

Re-calibration is recommended to be no more than 12 months from the date of this Certificate.
This Certificate and accompanying data shall not be reproduced, except in full, without the written
consent of Colorado Engineering Experiment Station Inc.

91

COLORADO ENGINEERING
EXPERIMENT STATION, INC.

```
Calibration of a Critical Flow Venturi
Model:  CFV-416-SPCL-10.000-2d-SPCLIF-CS/304      Serial Number:  9961
For:  Flow Systems, Inc.   Order:  8648
Data File:  97FSY353   Disc:  1197-027   Date:  17 November 1997
Inlet diameter: 26 inches    Throat diameter: 10 inches
Test gas: AIR    Standard density= .074915  lbm/cu-ft
  at standard conditions of 529.69 deg R, and 14.696 psia
Press: Inlet static pressure in psia
Temp: Inlet temperature in degrees Rankine
Cd: Coefficient of Discharge
Rey No: Throat Reynolds number
Flow: Mass flow in pounds per second
C*: Critical Flow Factor, dimensionless
Upstream Blockage was not present
```

L	Press	Temp	Cd	Rey No	Flow	C*
1	25.500	453.6	0.99140	7.0138E+006	4.9648E+001	0.6857
2	25.357	450.8	0.99218	7.0367E+006	4.9561E+001	0.6857
3	25.322	448.1	0.99313	7.0893E+006	4.9691E+001	0.6858
4	23.859	445.2	0.99350	6.7387E+006	4.6986E+001	0.6857
5	23.653	443.9	0.99346	6.7060E+006	4.6648E+001	0.6857
6	23.392	442.7	0.99234	6.6479E+006	4.6142E+001	0.6857

```
Average values for above results:
Temp: 447.37 Deg R       Viscosity: .00000089128 lbm/inch-sec
```

Bibliography

[1] Epstein A.H. *Short Duration Testing for Turbomachinery Research and Development.* In Second Int. Symp. on Transport Phenomena, Dynamics, and Rotating Machinery, Honolulu, HI, 1988.

[2] Guenette G.R. Epstein A.H. and Norton R.J.G. The mit blowdown turbine facility. In *ASME paper*, 84-GT-116. ASME, 1984.

[3] Guenette G.R. *A Fully Scaled Short Duration Turbine Experiment.* PhD thesis, Massachusetts Institute of Technology, 1985.

[4] Epstein A.H. Guenette G.R. and Ito E. *Turbine Aerodynamic Performance Measurements in Short Duration Facilities.* In AIAA/ASME/SAE/ASEE 25th Joint Propulsion Conference, AIAA-89-2690. AIAA, 1989.

[5] Kerrebrock J.L. *Aircraft Engines and Gas Turbines.* The MIT Press, second edition, 1992.

[6] NIST. *Tables of Thermodynamic and Transport Properties of Air, Argon, Carbon Dioxide, Carbon Monoxide, Hydrogen, Nitrogen, Oxygen, and Steam*, 1960.

[7] Doebelin Ernest O. *Measurement Systems, Application and Design.* McGraw-Hill, Inc., fourth edition, 1990.

[8] Cai Y. *Aerodynamic performance Measurements in a Fully Scaled Turbine* Master's thesis, Massachusetts Institute of Technology, 1998.

[9] Shang T. *Influence of Inlet Temperature Distortion on Turbine Heat Transfer.* PhD thesis, Massachusetts Institute of Technology, 1995.

[10] ASME/ANSI MFC-7M-1987 *Measurement of Gas Flow by Means of Critical Flow Venturi Nozzles.* An American National Standard, The American Society of Mechanical Engineers, 1987.

[11] ASME/ANSI MFC-2M-1983 *Measurement Uncertainty for Fluid Flow in Closed Conduits.* An American National Standard, The American Society of Mechanical Engineers, 1988.

[12] Johnson R.C. *Calculation of Real Gas Effects in Flow Through Critical-Flow Nozzles.* Journal of Basic Engineering 86(3)(1964):519-526.

[13] Suo M. *Turbine Cooling.* The Aerothermodynamics of Gas Turbine Engines, ed G.C. Oates. AFAPL TR-78-52, Air Force Aero Propulsion Laboratory, Wright-Patterson Air Force Base, Ohio.

[14] Brain, T.J.S., and J. Reid, *Primary Calibration oc Critical Flow Venturis in High-Pressure Gas.* Flow Measurement of Fluids, H. H. Dijstelbergen and E. A. Spencer, eds, North Holland Piblishing Co., Amsterdam, 1978: 54-64.

[15] NIST 14. *NIST Mixture Property Database.* Standard Reference Database 14, Version 9.08 (1992) Fluid Mixtures data Center, NIST Thermophusics Division 838.02, Boulder, Colorado.

[16] Friend, D.G. *Private Correspondance about NIST 14*, Summer 1997. Fluid Mixtures data Center, NIST Thermophusics Division 838.02, Boulder, Colorado.

[17] Denton, J.D. *Loss Mechanisms in Turbomachines.* ASME Journal of Turbomachinery, 115, pp. 621-656.

[18] Bender, E. *Equations of State Exactly Representing the Phase Behaviour of Pure Substances.* Ruhr-Univresity, Bachum, Germany.